LBL-11117

Lawrence Berkeley Laboratory
UNIVERSITY OF CALIFORNIA

Materials & Molecular
Research Division

THE HIGH TEMPERATURE BEHAVIOR OF METALLIC INCLUSIONS IN URANIUM DIOXIDE

Rosa Lu Yang
(Ph.D. thesis)

MASTER

August 1980

Prepared for the U.S. Department of Energy under Contract W-7405-ENG-48

THE HIGH TEMPERATURE BEHAVIOR OF METALLIC INCLUSIONS IN URANIUM DIOXIDE

Contents

ACKNOWLEDGMENTS

This thesis is not entirely my own individual effort. The advice and counsel from others concerning the research work as well as the encouragement and moral support from friends made this thesis possible. In particular, I would like to express my appreciation to the following people:

Professor D. Olander, who suggested this topic, whose excellent guidance and advice contributed heavily to this thesis, and whose enthusiasm and devotion toward research are always inspirational.

Professor L. Brewer, whose invaluable advice, constant accessibility, and patience for consultation are deeply appreciated.

Professor T. Pigford, whose comments on this thesis and whose serving on the thesis committee are appreciated.

Professor S. Prussin, whose invaluable discussions, understanding, concern, and encouragement are deeply appreciated.

I would like to thank my former colleague, Professor Albert Machiels of the University of Illinois, for his assistance in the experimental work during the early stages of research and for his encouragement and moral support during the final stages.

I would also like to thank my colleagues, Doug Dooley, Kee Kim, Shih-Hsiung Shann, Chuen-Horng Tsai, for the many fruitful discussions, for their assistance in the laboratory, and especially for their moral support. Their friendship made this almost a decade of graduate study possible. My special thanks go to Kee, who helped determine the stoichiometry of the sample.

I would like to thank Dr. R. Adamson and Mr. C. Berry of the General Electric Company, Vallacitos Laboratory, for providing the UO_2 samples used in this experiment. Their swift and excellent service is deeply appreciated.

I would like to thank John Souza and Dan Winterbauer for fabricating the numerous needed parts during the entire experiment, and Jack Harrel for prompt electronic support.

My thanks also go to Mr. B. Giauque for his excellent service in x-ray fluorescence counting, and to Mr. D. Newhart for the excellent machine work on refractory metals, often within an unreasonably short time limit.

The neat drawings by Gloria Pelatowski and the accurate typing of Carmen Hubbard and Deberah Craig are greatly appreciated.

Lastly, I would like to thank my parents, my husband, Cheh-Suei, my sister, Hong-Min, and my friends, Mei-Teh and Mike Hsu, for their everlasting encouragement, understanding, and moral support. Without them, I might have never completed this project.

This work has been sponsored by the United States Department of Energy under Contract W-7405-ENG-48, through Lawrence Berkeley Laboratory.

To my parents

THE HIGH TEMPERATURE BEHAVIOR OF METALLIC INCLUSIONS IN URANIUM DIOXIDE

Rosa Lu Yang

Materials and Molecular Research Division
Lawrence Berkeley Laboratory
and
Department of Nuclear Engineering
College of Engineering
University of California
Berkeley, California 94720

ABSTRACT

The object of this thesis was to construct a temperature gradient furnace to simulate the thermal conditions in the reactor fuel and to study the migration of metallic inclusions in uranium oxide under the influence of temperature gradient. No thermal migration of molybdenum and tungsten inclusions was observed under the experimental conditions. Ruthenium inclusions, however, dissolved and diffused atomically through grain boundaries in slightly reduced uranium oxide. An intermetallic compound (probably URu_3) was formed by reaction of Ru and UO_{2-x}. The diffusivity and solubility of ruthenium in uranium oxide were measured.

I. INTRODUCTION

A. Metallic Inclusions in Reactor Fuel

The fission products produced during irradiation can be divided into four groups: insoluble alkaline earth oxides, noble metal inclusions, soluble fission product oxide and elemental fission gases. Due to the high temperature and steep temperature gradient in oxide nuclear fuels, there is significant redistribution of the fission products after they are produced. The location and chemical state of the fission products influence the mechanical and thermal performance of the fuel[1,11] so it is important to investigate the behavior of these species in oxide fuels. In this thesis, the behavior of metallic inclusions under isothermal conditions and under the influence of the temperature gradient is investigated.

Postirradiation analysis[2-11,15,16] shows that metallic inclusions are distributed in the grain boundaries of the columnar grain and equiaxed grain regions in both uranium and uranium-plutonium oxide fuels. These metallic inclusions, usually smaller than 10 μm diameter, contain molybdenum, ruthenium, technetium and small amounts of palladium and rhodium.[6-9] Some papers even report uranium in the inclusions.[2,4,5] The concentration of each element in the inclusion is affected by the temperature, the oxygen potential, the burnup, and the type of fuel. Of the five elements found in the metallic inclusions, molybdenum is of special interest.[14] The oxygen potential of the Mo/MoO_2 couple is very

close to that of the stoichiometric uranium-plutonium oxide system; therefore molybdenum has a buffering action on the oxygen-potential of the fuel. The oxygen potential at the fuel-cladding interface determines whether fuel can react with cladding. Such reaction results in corrosion of the metal and consequent weakening of the cladding. Very little is known about the formation and the migration of metallic inclusions in uranium dioxide. However it is generally believed[12,13,17] that due to the steep temperature gradient in the reactor fuel, the metallic inclusions move bodily up the temperature gradient. Occasionally, big chunks of metallic fission products are found in the central void[10,15] which seems to support this belief. In order to predict the oxygen potential and thermal performance of the fuel element under irradiation, it is important to study the migration velocity and mechanism in detail. Two experiments have been performed previously in an effort to study this phenomena.

B. Related Work on Migration of Metallic Inclusions

(i) Annucci et. al.,[13] attempted to measure the migration velocities of molybdenum and ruthenium inclusions in both uranium and uranium - plutonium oxide in an out-of-pile experiment. Small metallic inclusions of molybdenum and ruthenium were coprecipitated in the oxide powders. The oxide pellets contained uniform distributions of metallic inclusions (all less than 0.3 μm diameter). The radial temperature gradient was created

by passing electrical current through the sample, which was held at central temperature as high as 3070°K for 15 min. After the heat treatment, inclusions as big as 10 μm diameter were found. The authors concluded that:

1. Surface diffusion was responsible for the movement of small inclusions, which caused coagulation of small inclusions to form large ones up to 10 μm in diameter.
2. Inclusion larger than 5 μm diameter do not migrate noticeably. However, there was no experimental data to support the surface diffusion theory and the experiment did not give any direct evidence of bodily migration of inclusions.

(ii) Poeppel et. al.,[12] tried to measure the migration velocities of metallic inclusions and bubbles in irradiated fuel. By etching polished metallographic sections from the irradiated fuel, they observed trails behind migrating second phase particles, which ranged in size from 0.5 μm to 5 μm diameter. The temperature range was 1600°C to 1850°C and the average temperature gradient was 5400°C/cm. A surface diffusion mechanism with a positive value for heat of transport was proposed. Although the trails seem to give direct evidence of migration, the data obtained scattered over a large range and there was a large discrepancy

between the data and calculated velocities based on surface diffusion mechanism.

C. Purpose of This Study

There are two approaches to analyzing the behavior of metallic inclusions in irradiated fuel. The first one is to examine the location and chemical form of fission products in highly irradiated fuel specimen by post-irradiation techniques, such as β and α autoradiography,[16] γ energy scanning or electron probe microanalysis.[2-10] This approach is very costly and time consuming. Another drawback of this approach is that the behavior of metallic inclusions in irradiated fuels depends on many interlinked parameters which are difficult to evaluate. The second approach is a more fundamental one in which the movement of metallic inclusions is studied under simplified, controlled conditions. In this thesis, we take the second approach.

The purpose of this experiment is to build a temperature gradient furnace to simulate in-pile thermal conditions and to study the high temperature behavior of metallic inclusions under the influence of a temperature gradient. We hope to clarify Poeppel and D'Annucci's work in this experiment, because our experimental design differs from theirs in the following ways. First, it is an out-of-pile experiment and only the thermal effect is present. Second, we have a definite starting plane for the inclusions as opposed to initial uniform distribution in previous studies.

II. THEORY

The object of this chapter is to define the basic quantities and to derive the equations describing the isothermal and thermal diffusion experiments performed in this thesis. Detailed treatments of the equations of irreversible thermodynamics can be found in Refs. 18-22.

The "Thermodynamic equation of motion" assumes linearity between fluxes and thermodynamic forces. The flux equation can be written as

$$\vec{J}_i = \sum_{k=1}^{n+1} L_{ik} \vec{X}_k \qquad (1)$$

where J_i is the flux of the ith species representing one of n particular atomic or molecular species or the heat flow,

$\vec{X}_k$ were the thermodynamic driving forces for species k,

L_{ik} are phenomenological coefficients.

There are no unique choices of variables for the various fluxes and driving forces. For our particular case of fluxes represented by heat and mass transport and forces due to gradients of the chemical potential and the temperature, the flux-force relations in a binary mixture of A and B are:

$$J_A = -L_{11}(\nabla \mu_A)_T - L_{1q} \frac{\nabla T}{T} \qquad (2)$$

$$J_q = -L_{q1}(\nabla \mu_A)_T - L_{qq} \frac{\nabla T}{T} \qquad (3)$$

In Eqs. (2) and (3), J_A is the mass flux of A, μ_A is the chemical potential of A, J_q is the heat flux, and L_{11}, L_{1q}, L_{q1}, L_{qq} are constants of proportionality. The Onsager theorem[20] requires that

$$L_{1q} = L_{q1}. \tag{4}$$

For ideal or dilute solutions the gradient of the chemical potential can be related to concentration by

$$\left(\frac{\partial \mu_A}{\partial C_A}\right)_T = \frac{kT}{C_A}. \tag{5}$$

Combining (2), (4) and (5), yields

$$J_A = - D_A \left(\nabla C_A + \frac{C_A Q_A^*}{kT^2} \nabla T\right) \tag{6}$$

where C_A is the concentration of species A. For volume diffusion C_A has units of cm^{-3}. For surface diffusion C_A is in units of cm^{-2}.

$D_A \equiv L_{11} \frac{kT}{C_A}$ is the diffusion coefficient, and

$Q_A^* \equiv \frac{L_{1q}}{L_{11}} = \left(\frac{J_q}{J_A}\right)_{\nabla T = 0}$

is called the heat of transport. It is the heat flux per unit mass flux of component A in the absence of a temperature gradient. It may be viewed as the average energy of the migrating species in excess of the heat content of the surroundings in which the migration takes place. It is an experimentally determined parameter which describe the direction and magnitude of the thermal diffusion (Soret) effect.

Equation (6) yields flux equations for each mobile species in a multi-component material. Thus for UO_2, flux for both U and O atoms are possible, each with its own Q^*. For the compound $A_X B_Y$, D and Q^* are

$$D = \frac{D_A D_B}{XD_B + Y D_A} \tag{7}$$

$$Q^* = X Q_A^* + Y Q_B^* \tag{8}$$

A. Atomic Diffusion

A-1. Isothermal Diffusion in a Binary System

In isothermal system, $\nabla T = 0$, Eq. (6) becomes

$$J = - D \nabla C \tag{9}$$

which is Fick's first law. The continuity equation states that

$$\frac{\partial C}{\partial t} = -\nabla \cdot \vec{J}. \tag{10}$$

Combining Eqs. (9) and (10), for a one dimensional system, yields

$$\frac{\partial C}{\partial t} = \frac{\partial}{\partial x}\left(D \frac{\partial C}{\partial x}\right). \tag{11}$$

For the initial and boundary conditions

I.C $\quad C(x, 0) = 0 \qquad$ For $x > 0$

B.C $\quad C(x_o, t) = C_o$

$\quad C(\infty, t) = 0$

The solution to Eq. (11) is

$$C(x,t) = C_o \operatorname{erfc}\left(\frac{x - x_o}{2\sqrt{Dt}}\right) \qquad (12)$$

A-2. Diffusion in a Thermal Gradient

For the case of atomic diffusion affected by both concentration and temperature gradients, as the case in section C-5 of chapter 3, the mass flux is described by Eq. (6). The equation that describes the system is

$$\frac{\partial C}{\partial t} = \frac{\partial}{\partial x}\left\{ D(T)\left[\frac{\partial C}{\partial x} + \frac{CQ^*}{kT^2}\frac{dT}{dx}\right]\right\} \qquad (13)$$

with I.C $\quad C(x, 0) = 0 \quad$ for $x > 0$

B.C $\quad C(x_o;t) = C_o$

$\quad C(\infty, t) = 0$

Equation (13) has to be solved numerically for $C(x, t)$.

B. Migration of Inclusions in a Temperature Gradient

The thermal migration of inclusions through the matrix may occur as a result of (1) purely thermal migration of atoms (Soret effect); (2) the flux of atoms caused by a concentration gradient arising from the thermal gradient. Mass transport may take place in either the inclusion, the matrix, or the matrix-inclusion boundary. The migration phenomena of inclusions were studied in great detail by Geguzin and Krivoglaz[23] and by Nichols.[24] In this thesis, we separate the inclusions into two

groups; the soluble and the insoluble inclusions and make the assumption that the interfacial kinetics are fast enough so that the migration process is controlled by diffusion.

B-1. Insoluble Inclusions

Insoluble inclusions are characterized by negligible mutal solubility of matrix and inclusion phases and $\nabla C_A = 0$ in Eq. (6). The presence of a temperature gradient will lead to the motion of matrix atoms in the vicinity of the inclusions in such a way as to make the inclusions move relative to lattice planes of the matrix, either up or down the temperature gradient. The thermal transport of matrix material can take place in either the matrix (external volume diffusion) or the inclusion-matrix boundary (surface diffusion).

(i) Surface Diffusion

As shown in Figure 2-1, the driving force created by a temperature gradient moves the host atoms around the inclusion, i. From Eq. (6), with $\nabla C_A = 0$ for insoluble inclusions, the surface flux J_s along the interface due to the temperature gradient, is[24]

$$J_s = - \frac{D_s Q_s^* C_s}{k T^2} (\nabla T)_\theta \qquad (14)$$

where D_s = interfacial diffusivity of UO_2, along the UO_2-inclusion interface,

Q_s^* = heat of transport of UO_2 for this process,

C_s = in units of cm^{-2}, surface concentration of UO_2 near the inclusion surface,

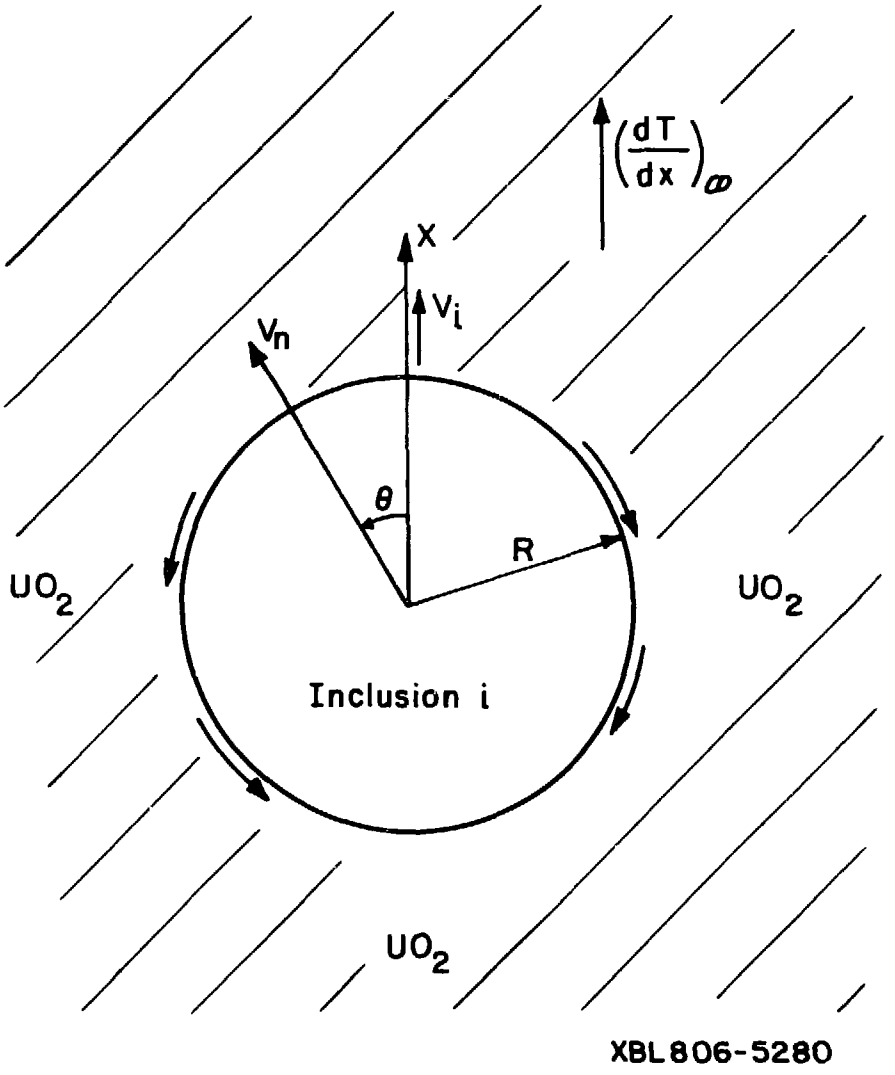

Fig. 2-1. Inclusion in the UO_2 matrix under the influence of temperature gradient.

$(\nabla T)_\theta$ = temperature gradient along the surface of inclusion.[24,25]

$$(\nabla T)_\theta = \frac{1}{R}\frac{dT}{d\theta} = -\beta_s \left(\frac{dT}{dx}\right)_\infty \sin\theta \tag{15}$$

$$\beta_s = \frac{3\, k_{UO_2}}{2\, k_{UO_2} + \{k_i/[1 + k_i (HR)^{-1}]\}} \tag{16}$$

β_s is a correction factor taking into account perturbation of the thermal gradient near the inclusions and H is the interfacial heat-transfer coefficient.[12]

k_{UO_2} = thermal conductivity of UO_2,

k_i = thermal conductivity of inclusion i,

$\left(\frac{dT}{dx}\right)_\infty$ = temperature gradient in the system far away from the inclusion.

Combining (14), (15), and (16) yields

$$J_s = \frac{D_s Q_s^* C_s}{k T^2} \beta_s \sin\theta \left(\frac{dT}{dx}\right)_\infty . \tag{17}$$

From the continuity equation, $\frac{\partial n}{\partial t} = -\nabla_s \cdot \vec{J}_s$, where $\nabla_s \cdot \vec{J}_s$ is the θ component of the surface gradient in spherical coordinates. $\frac{\partial n}{\partial t}$ is the change in number of UO_2 atoms along the surface of inclusion due to temperature gradient. Different numbers of UO_2 atoms arrive at the leading and trailing ends of the inclusion, thus making the inclusion move with a velocity V_i in the x-direction

$$V_i = -\frac{\partial n}{\partial t} \times \frac{1}{\cos\theta} \times \Omega = \frac{\Omega}{\cos\theta} \nabla_s \cdot \vec{J}_s \tag{18}$$

or

$$V_i = \frac{2 D_s \Omega^{1/3} Q_s^*}{k T^2} \left(\frac{\beta_s}{R}\right) \left(\frac{dT}{dx}\right) \tag{19}$$

where R = radius of inclusion,

Ω = molecular volume of the matrix atoms, UO_2.

The negative sign in Eq. (18) is due to the fact that UO_2 atoms and inclusions move in opposite directions. C_s has been approximated by $\Omega^{-2/3}$.

(ii) External Volume Diffusion

Due to the influence of temperature gradient, the matrix atoms move in the bulk of the matrix and causes the inclusions to move up or down the temperature gradient relative to the matrix. From Eq. (6), with $\nabla C_A = 0$ for insoluble inclusions,

$$J = - \frac{D_v C_v Q_v^*}{k T^2} \nabla T \tag{20}$$

where D_v = volume diffusivity of UO_2,

C_v = volume concentration of UO_2, in units of cm^{-3},

Q_v^* = heat of transport of UO_2 for volume diffusion,

∇T = temperature gradient at the inclusion,[24,25]

$$\nabla T = \left[1 - \frac{2(k_{UO_2} - k_i)}{2 k_{UO_2} + k_i}\right] \nabla T_\infty . \tag{21}$$

For volume diffusion,

$$\frac{\partial n}{\partial t} = -J_i \Omega = -J \cos\theta \, \Omega \tag{22}$$

where $\frac{\partial n}{\partial t}$ is the outward normal rate of motion of the surface, J_i is evaluated at the inclusion surface, and Ω is the molecular volume of the matrix material.

Combining Eqs. (20), (21), and (22), yields the velocity of the inclusion, with respect to the lattice

$$V_i = - \frac{D_v Q_v^*}{k T^2} \left[1 - \frac{2(k_{UO_2} - k_i)}{(2 k_{UO_2} + k_i)} \right] \nabla T_\infty . \tag{23}$$

For volume diffusion, as pointed out by Biersack and Diez[40] the lattice is itself moving at a velocity given by

$$V_\ell = \frac{D_v Q_v^*}{k T^2} (\nabla T)_\infty . \tag{24}$$

The net velocity of the inclusion for volume diffusion, V_v, with respect to the matrix material is then $V_i + V_\ell$

$$V_v = \frac{2(k_{UO_2} - k_i)}{2 k_{UO_2} + k_i} \frac{D_v Q_v^*}{k T^2} (\nabla T)_\infty . \tag{25}$$

B-2. Matrix Soluble in the Inclusions

Most thermomigration of gaseous and liquid inclusions fall in this category. Extensive studies, both theoretical and experimental, have

been done on migration of gaseous inclusions[24,26-30] (pores and voids) and liquid inclusions.[23,31-34] In this section, we only discuss the thermal migration of solid inclusions in solid.[35-44] The approximations involved in developing the migration formula for liquid and gaseous inclusions are different from those appropriate to solid inclusions. First, the interface kinetics is an important factor affecting the migration velocity for the gaseous and liquid inclusions, while for solid inclusions, the interface kinetics is so fast that diffusion is the rate limiting process. Second, for the liquid (and gaseous) inclusions, the temperature dependence of liquid (gaseous) diffusion coefficient is small compared with the variation of the mutual solubilities (vapor pressure) with temperature. However, in solid systems, the relative sensitivities of diffusivities and solubilities to temperature are reversed.

Consider a system, as shown in Fig. 2-2, the inclusion consists mainly of A. The matrix consists only of B. There is a temperature-dependent equilibrium solubility of B in A but A is insoluble in B. This provides a driving force for the migration of the inclusion in addition to that provided by thermal diffusion (Soret effect) as described in the preceding section. The two driving forces do not necessarily have the same sign. Mass flow may occur in either the interphase boundary or through the inclusion.

(i) Mass Transport in the Interphase Boundary

From Eq. (6). The mass flux of B in the interphase boundary is

$$J_B = -D_B \left(\nabla C_B + \frac{C_B Q^*}{k T^2} \nabla T \right) \tag{26}$$

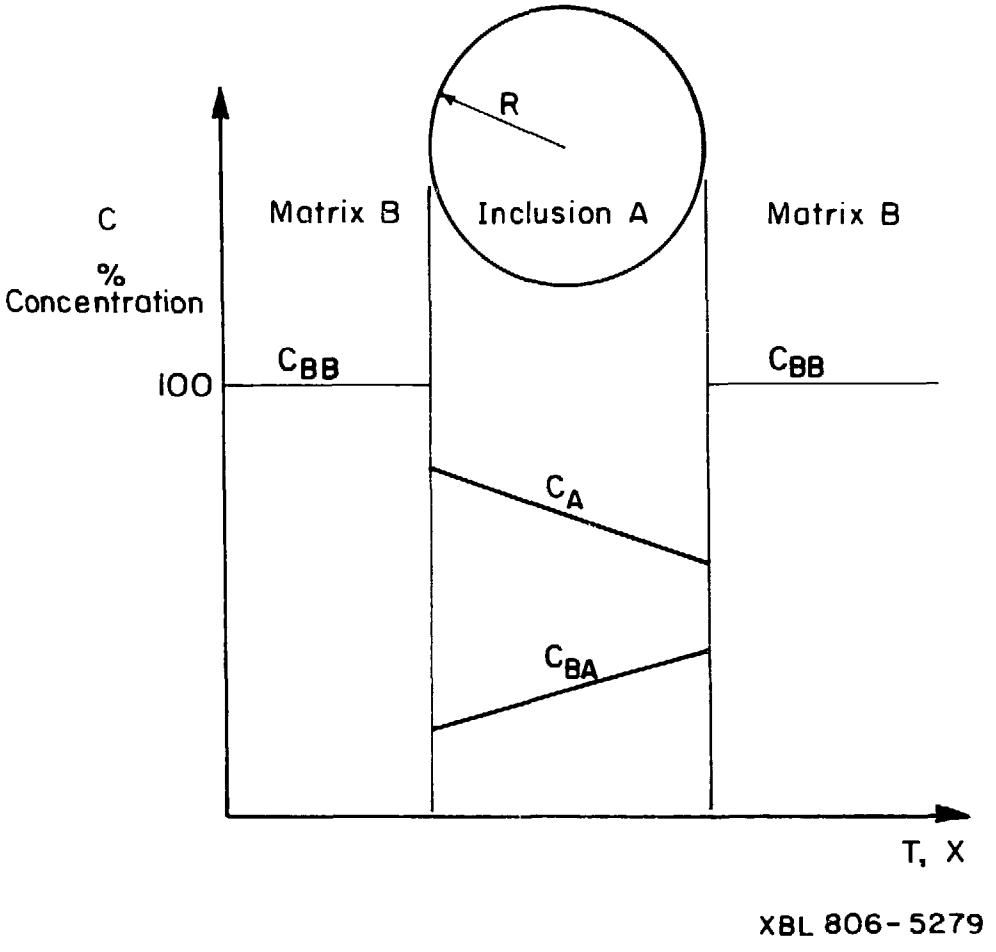

Fig. 2-2. Typical profile for the equilibrium concentration of elements A and B in an inclusion subjected to a temperature gradient.

where D_B = diffusivity of B in the interphase boundary,

C_B = concentration of B in the interphase boundary in units of cm^{-2},

Q^* = heat of transport for this process.

If we assume[45]

$$C_B = \frac{C_{BA} + C_{BB}}{2} \tag{27}$$

where C_{BB} and C_{BA} are the phase-diagram concentrations of B in the matrix and in the inclusion, combining (26) and (27), and assuming $C_{BA} << C_{BB}$ yields

$$J = -\frac{D_B}{2}\left(\frac{C_{BA}}{dT} + \frac{C_{BB}\,Q^*}{k\,T^2}\right)\nabla T \tag{28}$$

Using the relationship derived in Eq. (17) and (18), the migration velocity of the inclusion when mass transport is through the interphase boundary is

$$V = \frac{\Omega}{R}\left[D_B\left(\delta\,\frac{dC_{BA}}{dT} + \frac{C_{BB}\,Q^*}{k\,T^2}\,\beta_s\right)\left(\frac{dT}{dx}\right)_\infty\right]$$

$$= \frac{D_B\,\beta_s}{R\,C_{BB}}\left(\delta\,\frac{dC_{BA}}{dT} + \frac{C_{BB}\,Q^*}{k\,T^2}\right)\left(\frac{dT}{dx}\right)_\infty \tag{29}$$

where δ = is the thickness of the high diffusivity path,

Ω = the atomic volume of the matrix,

R = radius of the inclusion

$\left(\frac{dT}{dx}\right)_{\infty}$ = temperature gradient in the matrix far away from inclusion.

(ii) Mass Flow in the Inclusion

The migration of the inclusion is caused by solution of matrix material in the inclusion at the hot edge, diffusing through the inclusion and precipitating out at the cold edge of the inclusion. This is analogous to the vapor transport process in a pore.[24,27,29] With the same arguments as above, the mass flux through the precipitate could be described by

$$J = - \frac{D_B}{2}\left(\frac{d\, C_{BA}}{dT} + \frac{C_{BB}\, Q^*}{k\, T^2}\right) \nabla T$$

and the inclusion velocity is

$$V = - J \times \Omega = + \frac{1}{C_{BB}} \times \frac{D_B}{2}\left(\frac{d\, C_{BA}}{dT} + \frac{C_{BB}\, Q^*}{k\, T^2}\right) \nabla T$$

$$= \frac{1}{2}\left(\frac{D_B}{C_{BB}} \frac{dC_{BA}}{dT} + \frac{D_B\, Q^*}{k\, T^2}\right) \nabla T \qquad (30)$$

where D_B = diffusivity of B in inclusion,

C_{BB} and C_{BA} are the phase diagram concentrations of B in the matrix and in the inclusion,

∇T = temperature gradient in the inclusion,[24,32] and

$\nabla T = \left(\frac{3\, k_B}{2k_B + k_A}\right) \nabla\, T_{\infty}$.

B-3. Inclusions Soluble in Matrix

Consider the case of a spherical inclusion A with radius R in a matrix B. A temperature gradient ∇T is imposed on the system. A has some limited solubility in B and the equilibrium solubility of A in B, C_{AB}, is attained locally. Each A atom within the matrix experiences a force f_A due to the presence of temperature gradient:[24,31]

$$f_A = - k(\nabla T)\, \eta \tag{31}$$

where $$\eta = \frac{Q^*}{kT} + \frac{T}{C_{AB}\, m_B} \tag{32}$$

where Q^* = heat of transport,

m_B = the gradient of the solvus at the B-rich region of the A-B equilibrium diagram.

The first term in Eq. (32) is due to Soret effect; the second term is due to solubility driving force. The force f_A gives rise to a drift velocity V_A of A atoms relative to the B lattice[24]

$$V_A = \frac{D_A}{kT}\, f_A \tag{33}$$

D_A is the diffusivity of A in matrix B.

At steady state the depletion of A due to this diffusion process is compensated by the dissolution of additional A atoms at the A-B interface. This causes the displacement of the interface with a velocity,[38] V

$$V = - \frac{C_{AB} V_A}{C_{AA} - C_{AB}} . \tag{34}$$

Where C_{AA} is the equilibrium concentration of A in the A rich inclusion.

Combining (31) - (34) yields

$$V = \frac{C_{AB} D_A}{(C_{AA} - C_{AB}) T} \left(\frac{Q^*}{k T} + \frac{T}{C_{AB} m_B} \right) \nabla T \tag{35}$$

where[24,32]

$$\nabla T = \left(\frac{2(k_B - k_A)}{2k_B + k_A} \right) \nabla T_\infty$$

k_A and k_B are thermal conductivities of A and B, respectively.

III. EXPERIMENTAL

A. Material

A-1. Uranium Dioxide

The uranium dioxide samples used in this experiment were supplied by the General Electric Company. The pellets were made by the following technique: UO_2 powders were compacted into pellet shape with 30 000 psi pressure in a hardened tool steel die utilizing an uniaxial pressing technique. They were then fired in dry hydrogen (-83°C dew point) at 1680°C for 7 hrs. The pellets were centerless-ground to final dimensions. All pellets were ultrasonically cleaned in isopropyl alcohol and then dried in vacuum at 150°C for 16 hrs. Chemical analysis showed that the samples contained Si, B, Ca, Cr, Fe, Mo, Na, Cu, V, Zr, P, Ni, Al and Mg, all in the ppm range. No data on the carbon content are available.

The finished pellet is 98% of theoretical density and has an average grain size of about 15 μm. The photomicrograph of as-fabricated UO_2 sample, shown in Fig. 3-1, was obtained by grinding UO_2 with various grades of SiC paper, polishing to 1 μm diamond paste, then etching with a mixture of 10 mℓ H_2SO_4, 30 mℓ of H_2O_2, and 70 mℓ of H_2O for 5-10 minutes at room temperature to reveal grain boundaries.

A-2. Molybdenum, Tungsten and Ruthenium Powders

The fission product metallic inclusions found in reactor fuel are usually in the size range of 1-10 μm.[6,7] For convenience of detection

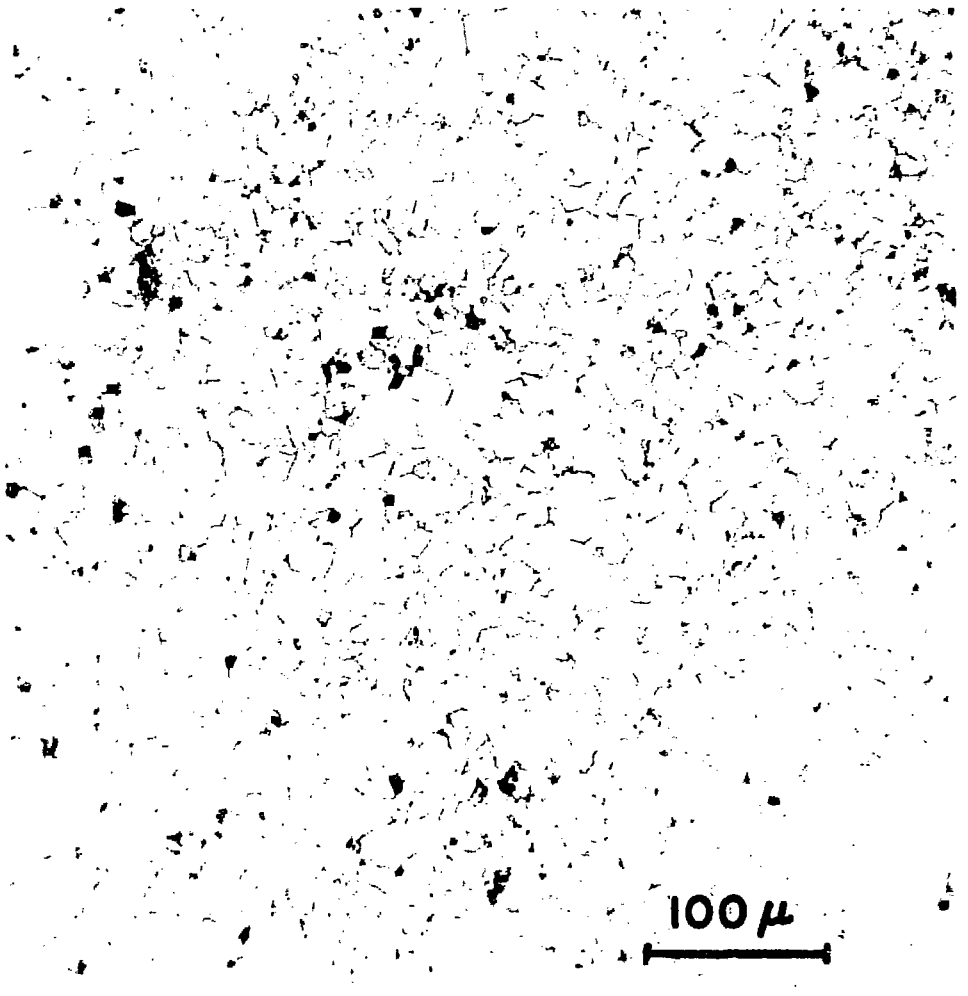

Fig. 3-1. Microstructure of as-received UO_2.

of the migrating inclusions from other inclusions which might be present as impurities in the UO_2 matrix, spherical particles about 5 μm in size were used whenever possible. Three different powders were used in this experiment: tungsten (supplied by Particle Information Service, Inc., Grants, Pass, Oregon), molybdenum, and ruthenium (both supplied by Western Gold and Platinum Co., a subsidiary of GTE Sylvania). Molybdenum and ruthenium were chosen because they are found in the fission product inclusions. Tungsten was used because of its compatibility with UO_2 and because it is available as spherical powders in the size range of 3-6 μm. Microphotographs of all three powders after deposition on polished UO_2 surfaces are shown in Figs. 3-2, 3-3, and 3-4. In Fig. 3-4, the black area around the ruthenium powders is the organic dispersant used in dispersing the powders. Pertinent properties of the powders are shown in Table 3-1.

A-3. Crucibles

A crucible is needed to encapsulate the UO_2 sample to avoid excessive evaporation loss at high temperature. The crucible material must meet the following requirements: 1) It must be metallic to permit heating by electron bombardment. 2) It must sustain temperatures as high as 2600°C. 3) It must be compatible with UO_2 in vacuum at high temperature. Possible candidates include molybdenum, tantalum, tungsten and rhenium. Rhenium is most chemically inert and has a high melting point, but is too expensive. Molybdenum and tantalum are relatively cheap and easy to fabricate. Molybdenum could not be used for experiments with temperature above 2500°C. Tantalum was abandoned because it reduces the UO_2 samples to highly substoichiometric oxide, which is undesirable.

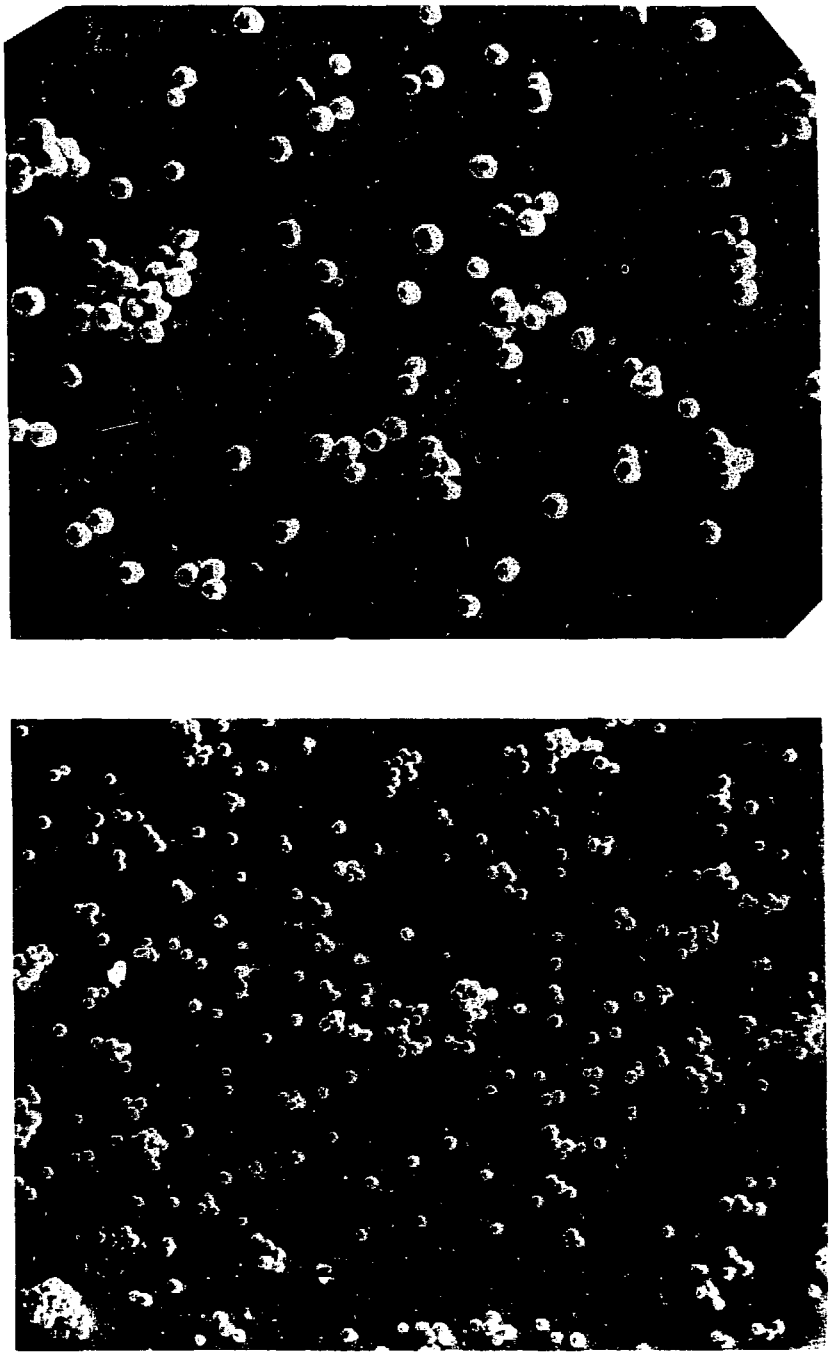

XBB 806-7286

Fig. 3-2. Scanning electron microscope picture of tungsten powders deposited on polished UO_2 surface.

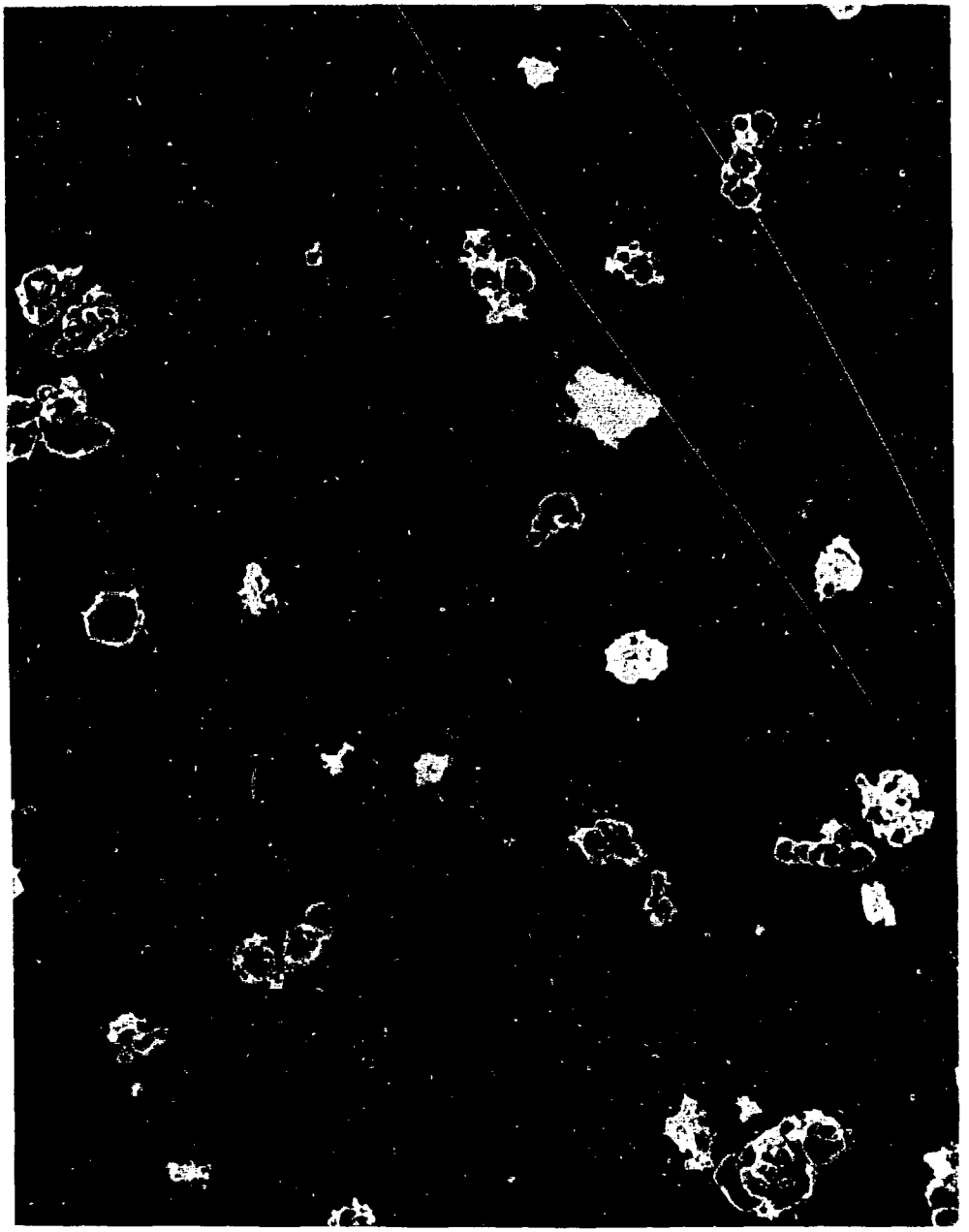

Fig. 3-3. Scanning electron microscope picture of molybdenum powders deposited on polished UO_2 surface.

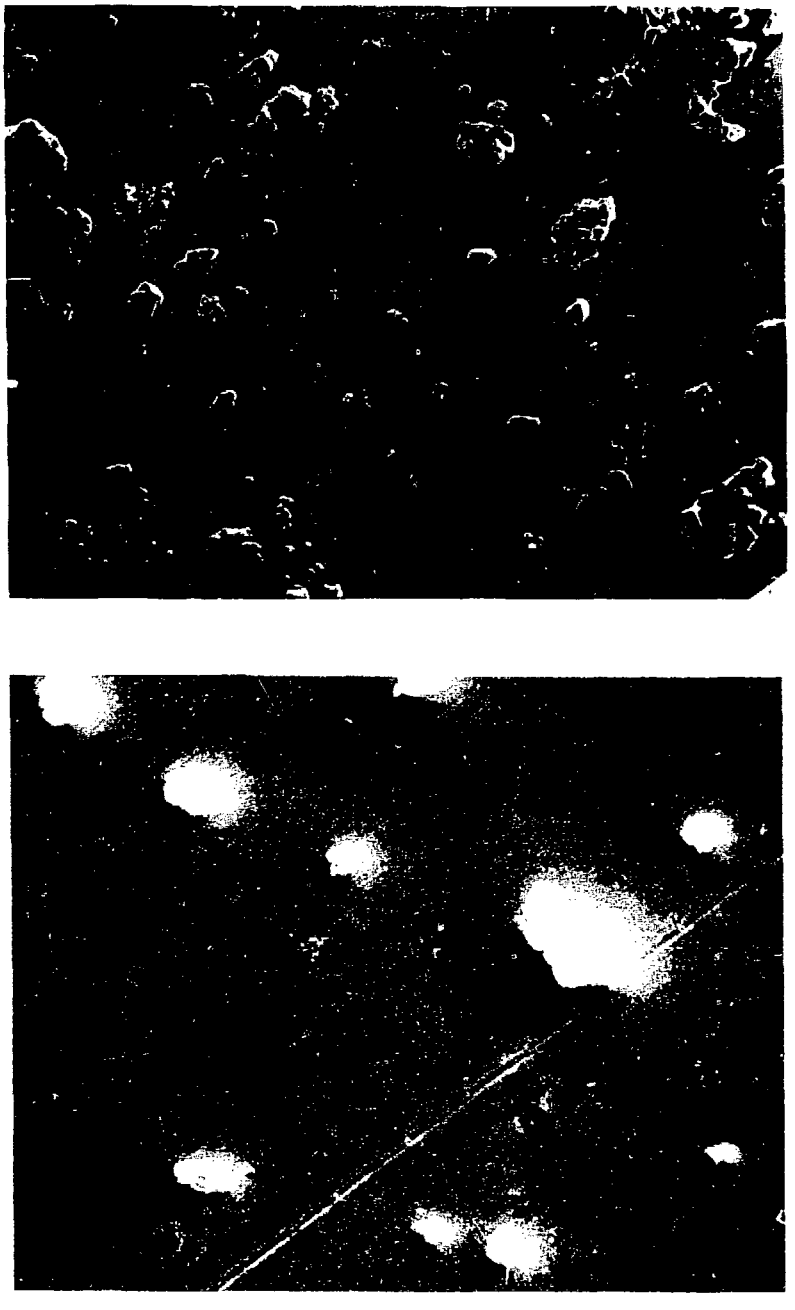

XBB 806-7285

Fig. 3-4. Scanning electron microscope picture of ruthenium powders deposited on UO_2 surface.

Table 3-1. Properties of molybdenum, tungsten and ruthenium powders.

	Molybdenum	Tungsten	Ruthenium
Particle shape	spherical	spherical	irregular
Particle size	1 - 5 μm	3 - 6 μm	over 90% 1 - 10 μm
Impurity content	not available	not available	Ag, CA, Fe, Pd, Rh, Al, Cu, Mg, Si
Melting point	2610°C	3410°C	2310°C

Thus leaves us only with tungsten. It is very difficult to machine tungsten crucibles to the desired tolerances. Initially, chemical vapor deposition (CVD) tungsten tubes were purchased from Ultramet Company, then a tungsten lid was electron beam welded to the tube to make a crucible. Later, integral CVD-fabricated crucibles (tube and lid) were used. (See section B-2 of this chapter for description).

A-4. Sample Preparation

The uranium dioxide pellets are centerless-ground to 1.186 cm diameter for fit into the tungsten crucible leaving a radial gap about 30 μm. This tight fit is necessary to avoid excessive evaporation loss of UO_2 in vacuum. A 0.15 cm thick wafer is sliced off each pellet using a thin diamond wafering blade (Buehler Company, Isomet low speed saw #11-1180). The wafer thickness is thin enough that the temperature in the wafer is sufficient for the inclusions to move at a reasonably high rate, yet thick enough for the migration distance to be easily measureable. The height of the remainder of the pellet is about 1.25 cm. To make the end surface of pellet and wafer smooth and parallel to each other, both end surfaces are first ground on 320, 400 and 600 SiC paper, using water as lubricant, and finally polished with 6 μm diamond paste, using Buehler Isocut fluid as lubricant. A layer of metallic powder is deposited on the UO_2 surfaces by the following method: Two drops of Triton X 100 (a dispersant made by Rohn and Haas) are mixed with ~ 0.1 gm of metallic powders and 40 mℓ of methyl alcohol in a 100 mℓ beaker. The beaker is then placed in an ultrasonic cleaner for 5 minutes

to shake loose the agglomerated particles. Immediately after turning off the ultrasonic cleaner, a polished UO_2 pellet (or wafer) is placed in the solution for ~20 seconds to collect a layer of metal powders. After taking the UO_2 pellet out of the solution, the pellet is allowed to dry slowly in a tight container so that the separated particles do not coagulate during the drying process. This deposition process is repeated several times to obtain a layer of individually separated powders of the desired density on the UO_2 surface. A typical photomicrograph of the UO_2 surface with tungsten powders is shown in Fig. 3-2. After the deposition of tungsten or molybdenum powders, the UO_2 wafer is placed on top of the pellet, and the whole sample is isothermally annealed as described below, then gently pushed into the crucible shown in Fig. 3-9. For the ruthenium thermal gradient experiment, the isothermal annelaing step is omitted.

B. Apparatus

B-1. Isothermal Sintering-Reduction Furnace

The reasons for sintering the UO_2 samples isothermally before the thermal migration experiments are: 1). To control the stoichiometry of the sample to avoid oxidizing the metallic inclusions in the subsequent thermal migration experiment. 2). To sinter the metallic inclusions with UO_2, so that they are well-embedded into the UO_2 matrix. Incomplete closure of the gap between the inclusions and the UO_2 matrix might impede the motion of the inclusion in the subsequent thermal migration experiment. 3). To densify and reduce the porosity in the UO_2 sample, thus reducing the

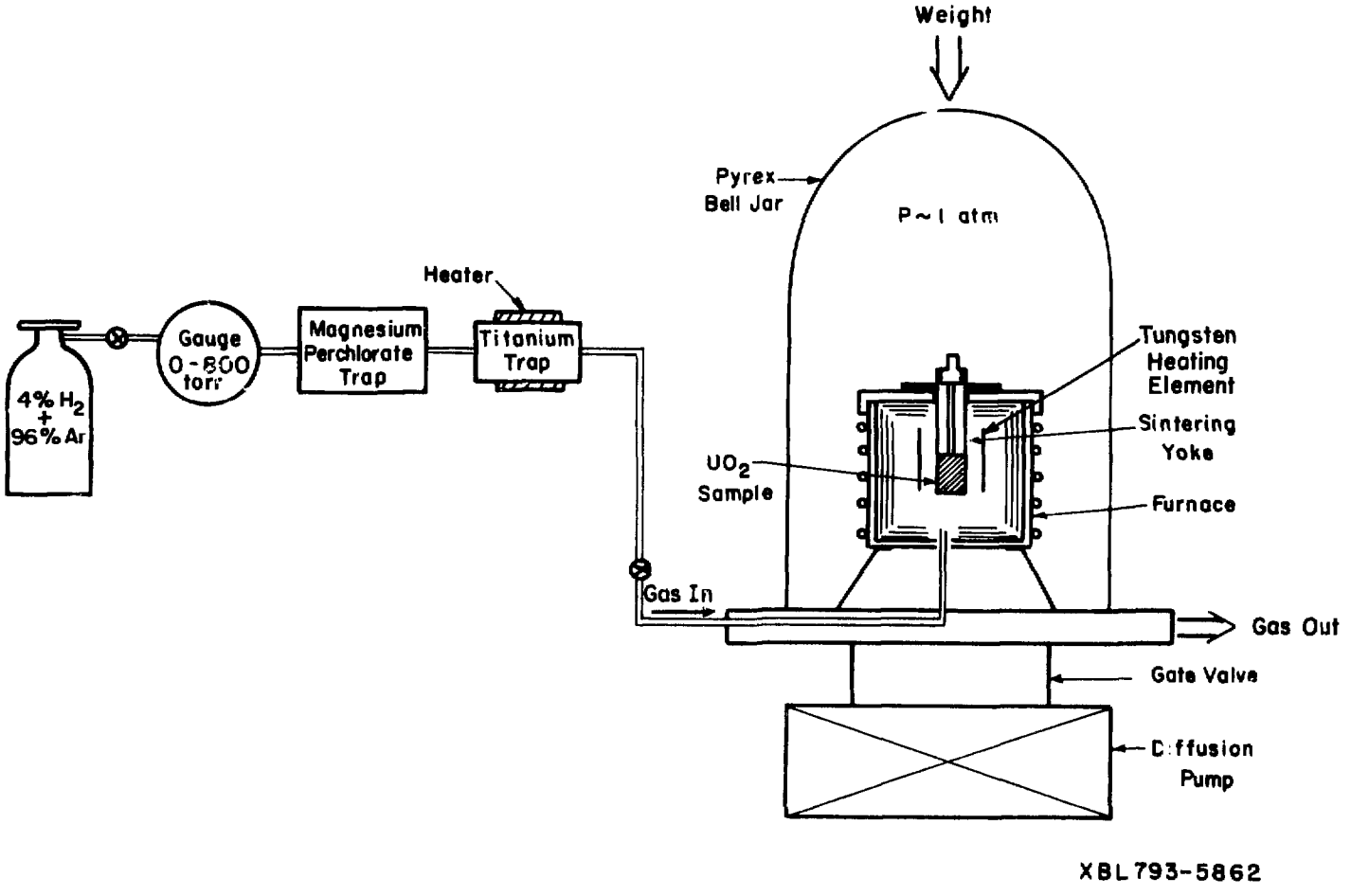

Fig. 3-5. Isothermal sintering-reduction apparatus.

size of the void formed at the tungsten lid by pore migration. (Section C-2 of this chapter). The isothermal sintering - reduction system consists of two parts, a gas purifying system and a sintering furnace to heat a yoke in which the samples are held.

(i) Gas Purifying System

A mixture of 4% H_2 and 96% Ar is used in the isothermal sintering procedure. Gas is fed into the system through 1/4-inch stainless steel tube, which was baked for 20 hrs each time before using to eliminate any water that might be adsorbed inside the tube. To eliminate oxygen and water, the feed gas was passed through two traps before it was fed to the furnace. As shown in Fig. 3-5, a magnesium perchlorate trap was used to remove the bulk of the water in the gas, and a titanium trap, which was heated to 700°C, was used to remove residual water and any oxidizing elements. The inlet gas was fed to the furnace through a 1/4-inch hole on the bottom of the furnace. The gas passed by the sample and was exhausted through a valve located at the bottom of the bell jar. Gas flow rates of ~ 2 C.F.H. were employed.

(ii) Sintering Furnace and Yoke

The sintering - reduction experiment was performed in a pyrex bell jar at a pressure slightly higher than atmospheric pressure to avoid in-leakage of air into the bell jar. The furnace which is situated in the bell jar, consists of a resistively heated Brew tungsten mesh (~ 7.5 cm in diameter and 15 cm long). Radiation shields of tungsten

and molybdenum surround the heating element. The yoke is inserted to the furnace through a top opening (as shown in Fig. 3-5). The temperature of the furnace is measured by both a W3Re-W25Re thermocouple placed close to the sample and by an optical pyrometer to which appropriate corrections for the prism, the bell jar and non-black body conditions were applied.

The sintering yoke (Fig. 3-6) is made of 1/8-inch thick wall molybdenum crucible with a tantalum nut at the top. Inside the molybdenum yoke, a tungsten or molybdenum alignment tube holds three UO_2 samples in place for annealing. Each UO_2 sample, separated from the others by a tungsten or molybdenum disks, consists of a UO_2 wafer and a UO_2 pellet with metallic inclusions in between. A molybdenum push rod exerts pressure on UO_2 samples when the tantalum nut on top of yoke is tightened. In order to place the UO_2 samples under high stress to deform plastically and close the pellet-wafer gaps, a 12.5 foot-pound torque is applied to the tantalum nut on the yoke at room temperature. At elevated temperatures, differential thermal expansion of the UO_2 and the metals should increase the compressive stress.

After the samples are placed in the furnace, the bell jar is pumped down to 1×10^{-6} Torr vacuum and baked at 500°C for about 2 hrs. Then the 4% H_2 and 96% Ar gas mixture is admitted to the system until the pressure reaches 780 Torr. In the meantime, the temperature of the furnace is increased slowly ($\sim$ 20°C/min) to avoid cracking the UO_2 samples. After the desired temperature is reached, annealing is continued for 10-36 hrs. During cool down, the gas is changed to pure argon to avoid

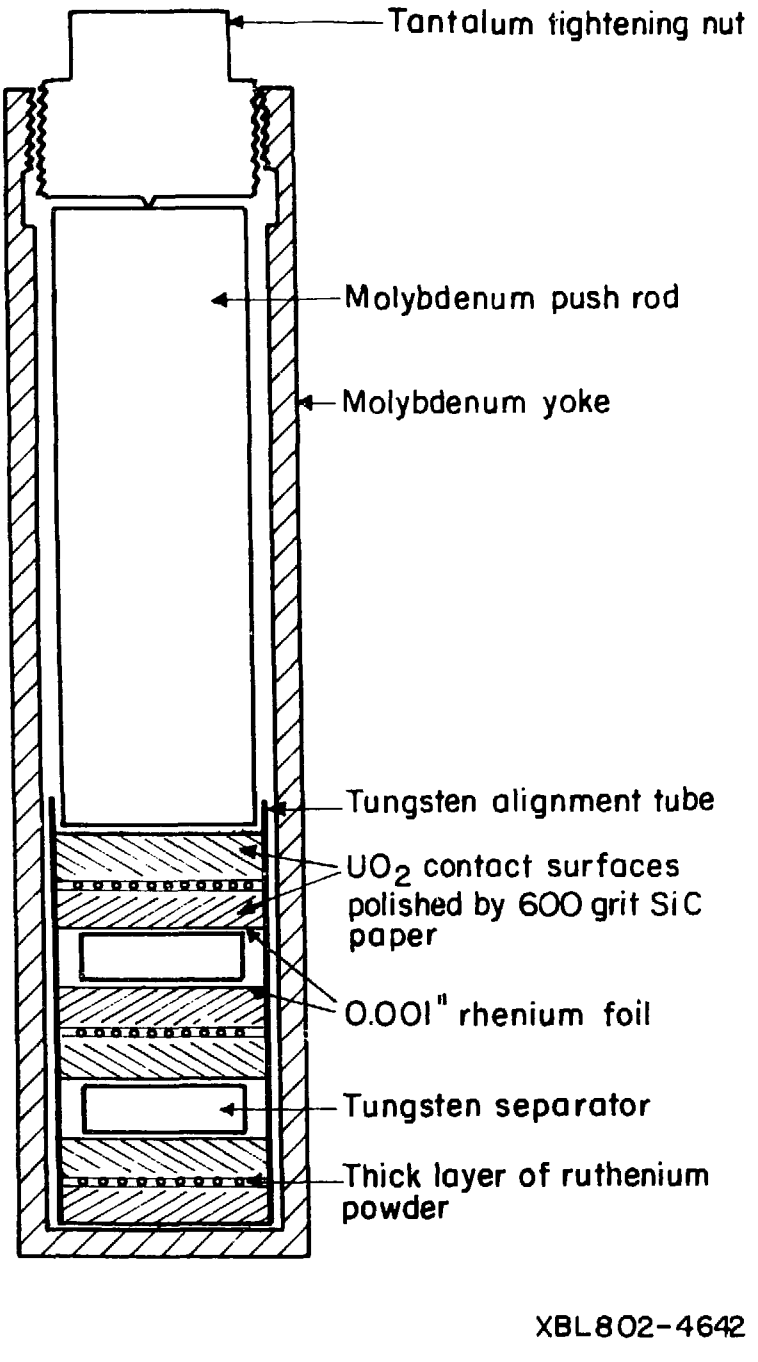

Fig. 3-6. Yoke for sintering of UO_2 samples. The alignment tube and separators were either of molybdenum or tungsten.

hydride formation by hydrogen reaction with the uranium precipitated from the substoichiometric uranium oxide. If the hydride forms, complete disintegration of the sample occurs. Figure 3-7 shows that after sintering, the pellet-wafer gap completely disappears and the metallic inclusions are well-embedded in the UO_2.

B-2. Temperature Gradient Furnace

A furnace which is capable of producing a temperature gradient of 1500°K/cm at a maximum temperature of 3000°K and keeping the UO_2 sample under compression at temperature is shown in Fig. 3-8.

The UO_2 sample (9) is contained in a tungsten crucible (5) with an integral top lid (all CVD fabrication) in which a 1 mm diameter, 6 mm long radial hole (6) is drilled by spark discharge for temperature measurement by optical pyrometry. To avoid chemical reaction between UO_2 and tungsten crucible at the highest temperatures, a rhenium foil (0.001 inch thick) is placed between the top of UO_2 sample and the bottom of tungsten lid. After the UO_2 sample is inserted into the tungsten crucible, a tantalum collar (12) is electron beam welded to the bottom of the crucible. The specimen-crucible assembly is shown in Fig. 3-9.

A tantalum push rod (14) is then inserted into the tungsten crucible containing the UO_2 sample. The tantalum yoke (15) holds the tungsten crucible down while the stainless steel nut (18) forces the tantalum push rod against the bottom of UO_2 sample to keep it in close contact with the bottom of lid of the tungsten crucible. A stainless steel spring (19) between the nut and the collar (17) ensures that the UO_2 sample is in compression at hight temperature. The top of the

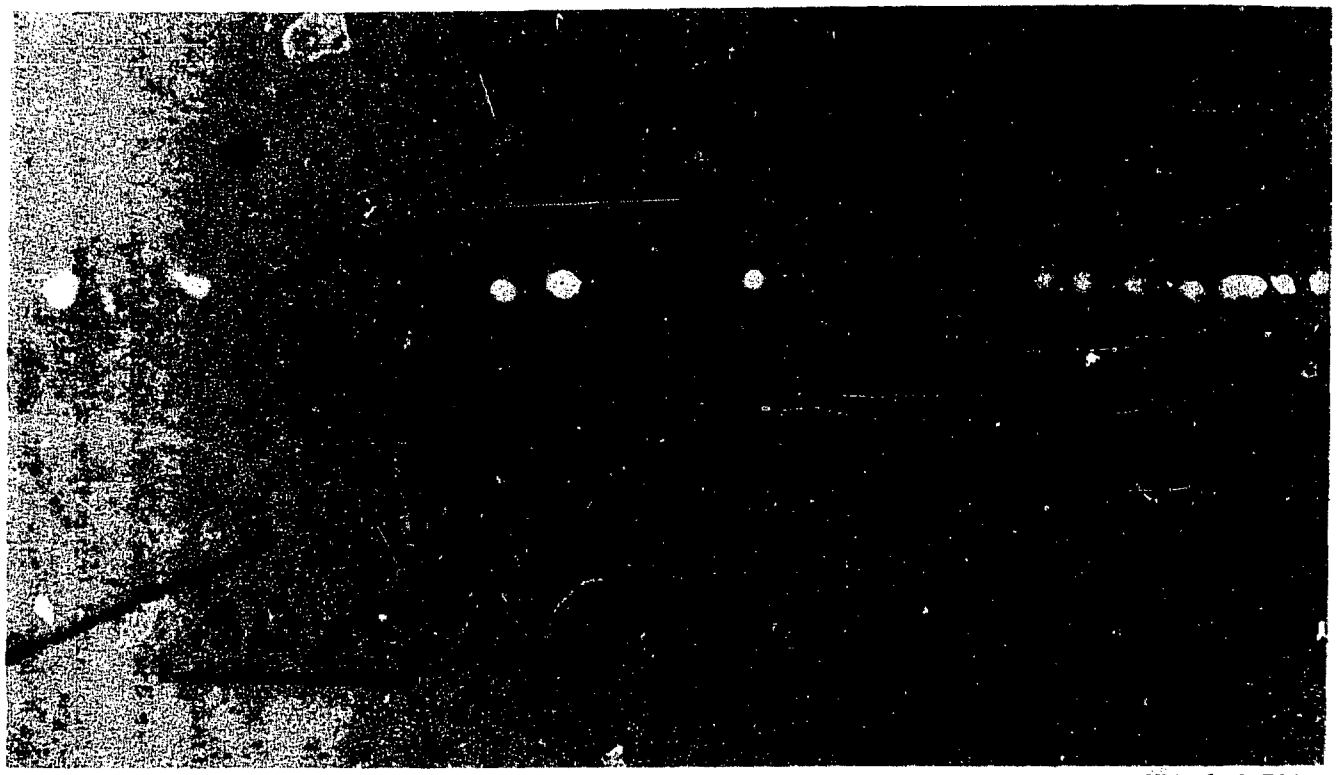

XBB 807-7913

Fig. 3-7. Microphotograph of wafer-pellet interface; the white dots are inclusions.

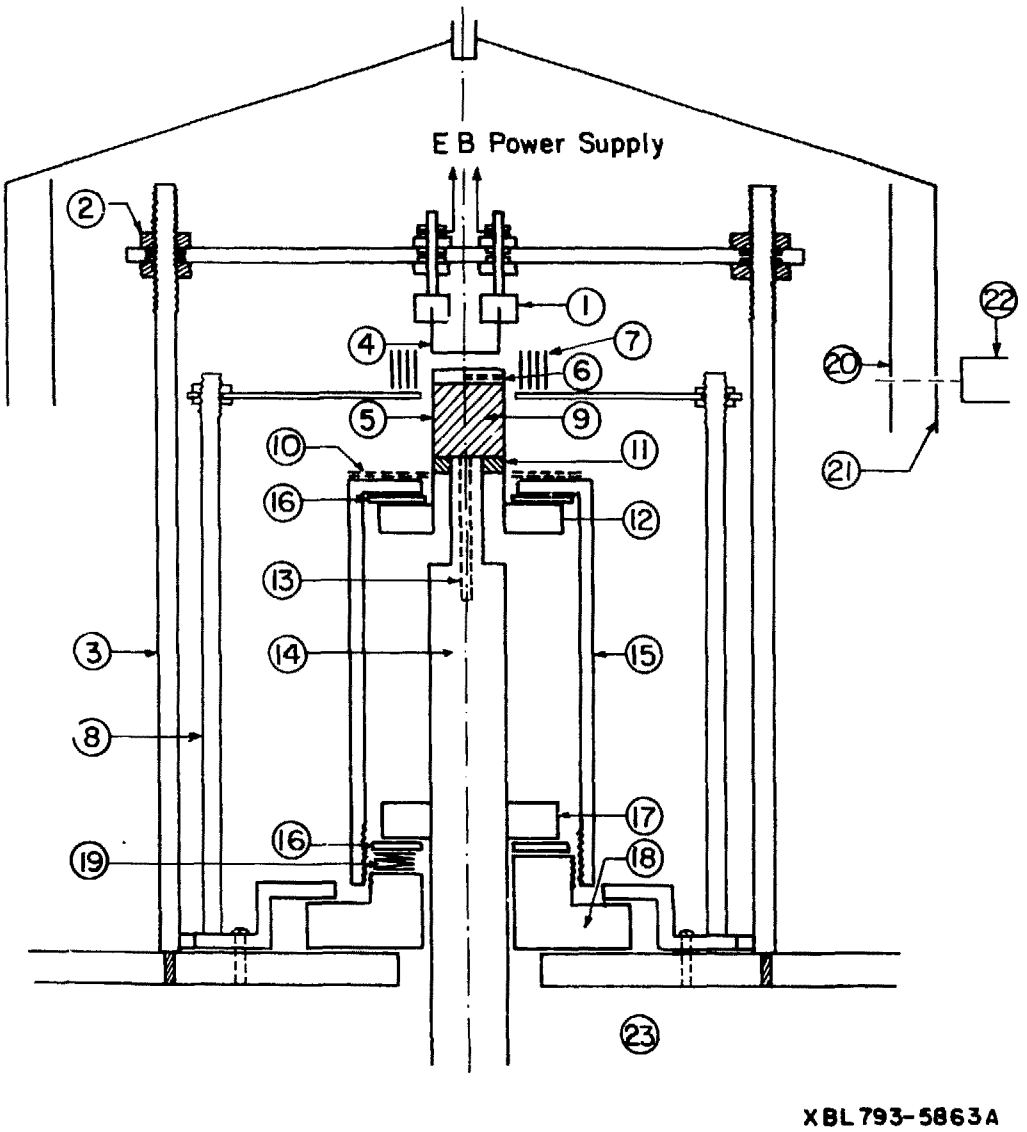

Fig. 3-8. Temperature gradient furnace.

Notes to Fig. 3-8:

1. filament holder
2. high purity alumina insulator
3. stainless steel post
4. tungsten filament
5. tungsten crucible (Fig. 3-9)
6. black body hole ($\ell/d \simeq 5$)
7. thermal shield floating at filament potential
8. ceramic post
9. sintered UO_2 sample (Fig. 3-9)
10. tantalum radiation shield
11. tantalum partial sleeve
12. tantalum collar
13. W-Re thermocouple
14. tantalum push rod
15. tantalum yoke
16. alumina washer (heat insulator)
17. molybdenum collar
18. stainless steel nut
19. stainless steel spring
20. shield
21. rotary glass shield
22. pyrometer
23. Brew furnace

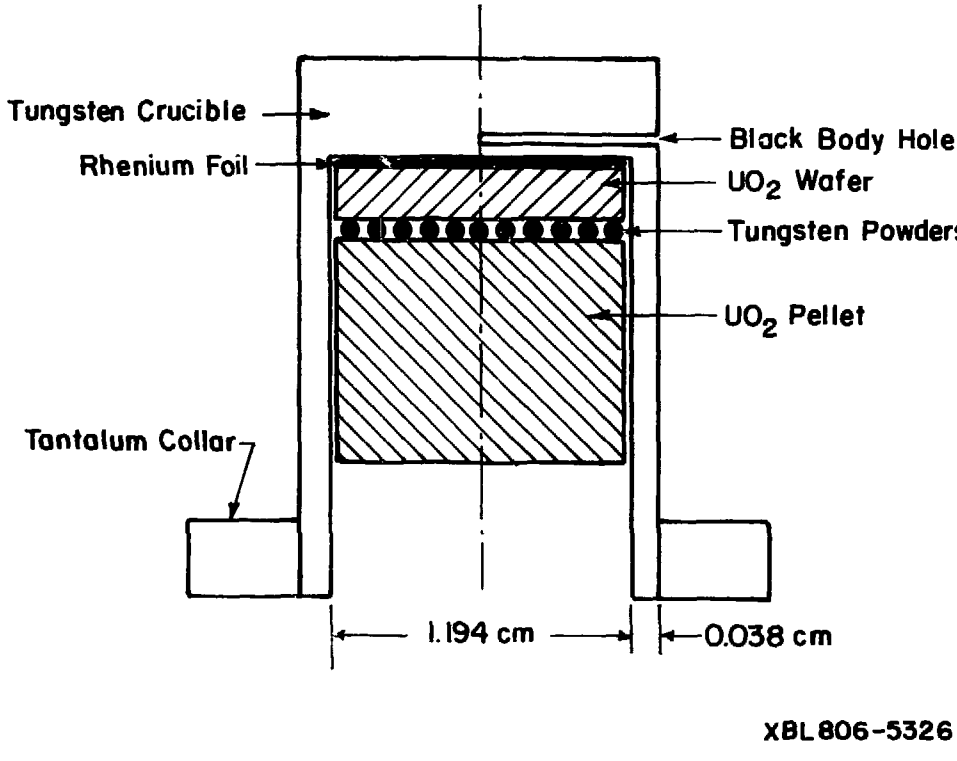

Fig. 3-9. Tungsten crucible with uranium dioxide sample.

tungsten crucible is heated by electron bombardment from a 0.051 cm thick flat spiral-wound tungsten filament (4), which is 3 mm away from the top of tungsten crucible and is at negative high voltage (between - 600 V to - 1000 V). Several layers of 0.005 cm thick concentric tantalum shields (7) float at the same potential as the filament to reduce the radiation heat loss from the top lid of the crucible. This shield eliminates the temperature gradient radially in the top lid and makes the temperature uniform along the inner wall of black body hole (6). The bottom temperature is established by heat conduction from the UO_2 pellet and the crucible wall to the tantalum push rod. To make the bottom temperature of UO_2 pellet uniform radially, a tantalum partial sleeve ring (11) is placed between the top of tantalum push rod and the tungsten crucible. The bottom temperature of UO_2 sample is measured by an ungrounded W3Re/W25Re tantalum - sheathed thermocouple with a 90° bend, which is inserted into a slot in the tantalum push rod and touches the bottom of the pellet. Radiation shields (10) and an alumina insulator (16) keep the yoke cool. If the yoke becomes hot and expands, it loses its ability to keep the specimen in compression.

A stainless steel dome-shaped shield (20) with a 1/4-inch hole and a rotary carousel (21) with about 50 glass slides on it are used to protect the inside bell jar surface in the viewing path from being coated, so that the top temperature can be measured by an optical pyrometer (22) periodically during the experiment.

B-3. Analysis Tools

Several detection tools were used frequently in analyzing the samples: An optical microscope, a scanningly electron microscope with EDAX, an electron microprobe and an x-ray fluorescence spectrometer. In this section, the basic principles of each device and its relation to the experiment are discussed.

(i) Optical Microscope

A Zeiss reflected light microscope with differential interference contrast feature was used to examine the microstructure of the polished UO_2 samples after the sintering experiments and to check the extent of migration of inclusions in UO_2. The limitations of the optical microscope are: 1. The depth of focus is limited to about 1000 Å, so only a portion of polished surface appears in focus. 2. Only the phase contrast is shown, so the ideality and composition of each phase is not known.

(ii) SEM (Scanning electron microscope) with EDAX (energy disperse analysis of x-rays)

The basic principle behind the operation of the SEM is the use of a fine electron beam striking the specimen. At the point of impact, a variety of phenomena occur, including production of secondary electrons, characteristic x-rays, auger electrons, etc., which can be used to obtain information on the specimen surface. By scanning the electron beam in a raster pattern across the specimen surface in synchronization with a cathode x-ray tube, it is possible to map the specimen surface onto the display system. In EDAX, by using a energy dispersive spectrometer, the

identity and concentration of each element can be measured by the intensity of their characteristic x-rays. SEM has higher resolution, higher magnification (X30 000) and greater depth of focus than the optical microscope. Combining SEM and EDAX, we have an excellent tool to examine the topology and the elemental composition of the specimen surface. However, since the image is produced by the scattered secondary electrons, it is very difficult to find a metallic inclusion in the UO_2 matrix. In optical microscopy, the two phases have very different reflectivities, and are easy to distinguish.

(iii) Electron Microprobe

The electron microprobe is similar to SEM but the induced characteristic x-ray is analyzed by wavelength spectrometer. The advantage of the microprobe over SEM and EDA for our purpose is the availability of an optical microscope inside the vacuum system, which permits observation of the sample optically and determination of the elemental composition simultaneously. The disadvantage is that the resolution of our machine is very low. We used this machine to identify the elements in the metallic phase in UO_2 sample for ruthenium annealing experiments, but it was impossible to obtain quantitative information.

(iv) X-ray Fluorescence Spectrometer

The x-ray system shown in Fig. 3-10 was designed, constructed and operated by the Instrument Technique Group at Lawrence Berkeley Laboratory. It consists of a low power tungsten - anode x-ray tube, a silver secondary target to provide nearly monochromatic secondary excitation radiation, a

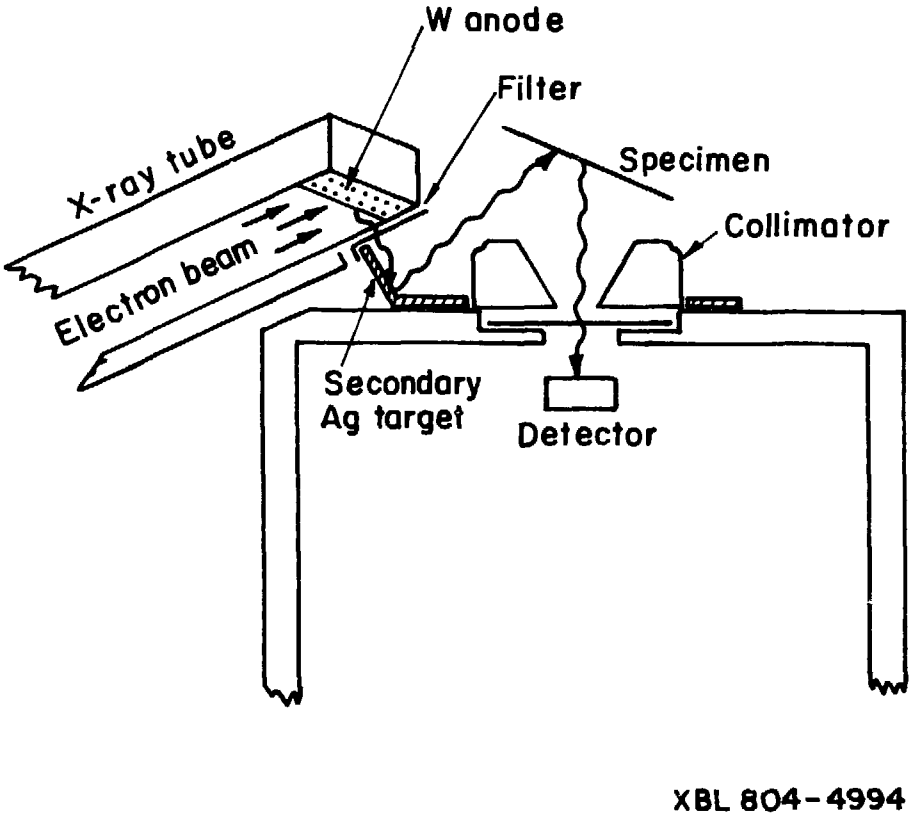

Fig. 3-10. X-ray system used in x-ray fluorescence spectrometry.

silicon guard-ring reject detector and a 1024 channel pulse height analyzer. The purpose of this instrument is to measure the concentration of certain elements over a large area (~ 1.2 cm in diameter). After the annealing experiments described in section C-4 and C-5 of this chapter, we used x-ray fluorescence spectrometry to determine the surface concentration ratio of ruthenium and uranium by monitoring the K_α x-rays from ruthenium and the $L\gamma_1$ radiation from uranium.

C. Experimental Development

C-1. Initial Results

Several experiments were carried out in a somewhat more primitive version of the temperature gradient furnace shown in Fig. 3-8. Molybdenum and tungsten particles were used as inclusions. The top of crucible was heated to about 2600°C at black body hole. The temperature of the bottom of the UO_2 pellet was about 1000°C. The temperature gradient in the UO_2 sample was about 1000°C/cm. The thermal gradient anneal for each experiment lasted about 10 hrs. Following the thermal gradient heat treatment, we first cut the tungsten lid off tungsten crucible, using a diamond saw and a spark cutter, to remove the UO_2 sample. Then the specimen was sectioned longitudinally, mounted in plasimont (by Buehler Co.), ground with 120, 240, 320, 400, 600 grit SiC paper and finally polished with 6 μm and 1 μm diamond paste to achieve an optically smooth surface. After the sample was prepared by the above method, it was observed with the optical microscope to determine the migration distances and sizes of the inclusions. The grinding/polishing process was repeated several times

times to obtain good statistical results by uncovering additional inclusions. Also, the sample was etched after polishing to reveal the microstructure of the sample.

There were several interesting aspects observed from these experiments. As shown in Fig. 3-11, the sample exhibited remarkable reconstructing after thermal gradient heat treatment. Several process, including sintering, grain growth, and pore migration, occurred. In Fig. 3-11, four structural zone can be identified: 1. Unrestructured zone. At the cold end of the sample, the grain size is about the same as the sintered sample before thermal gradient heat treatment. 2. A grain growth zone. Grains became gradually larger toward the high temperature side. 3. Zone of elongated grains. These grains are similar to the columnar grains in reactor fuel. The extent of this zone is a function of temperature and heating time and differs from sample to sample. 4. A concave gap. As shown in Fig. 3-12, a gap (the black area at the top of the sample) is formed on top of the UO_2 sample during the thermal gradient experiment. The curvature of the gap outlines an isotherm at the top of UO_2 wafer. The gap arises from porosity in the UO_2 sample (which was not completely eliminated by the isothermal sintering step) and the residual gap left after the sintering procedure in between the UO_2 wafer and pellet. Both of these void sources migrate to the hot lid under the influence of temperature gradient and form the gap.

Besides these observations from etched samples, polished, unetched samples showed apparent inclusion migration. Spherical tungsten particles $\sim$ 5 μm in diameter were observed at the hot end of UO_2 sample

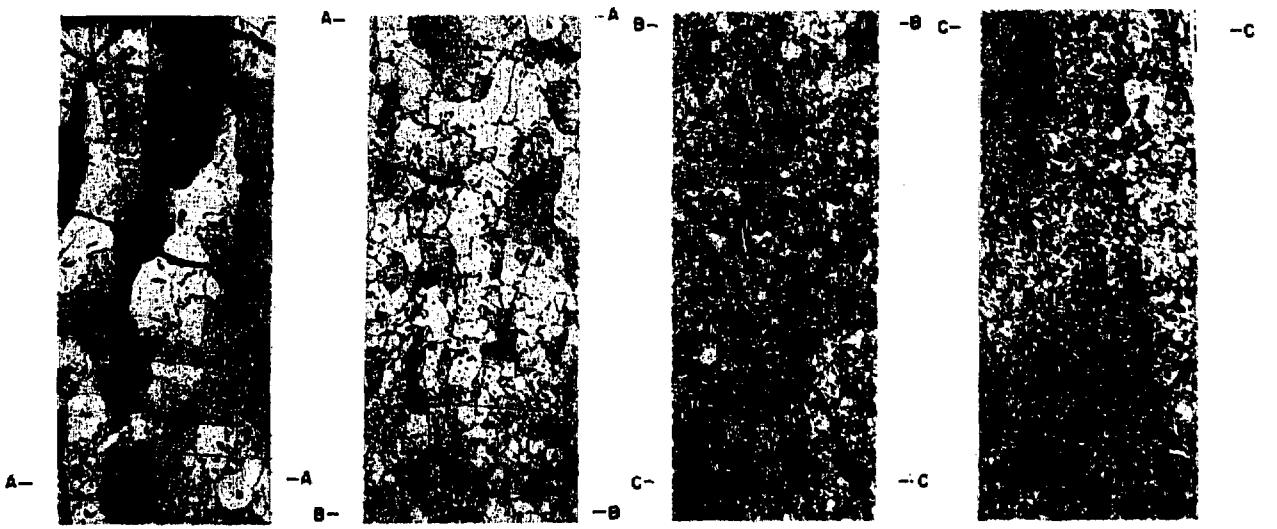

Fig. 3-11. Microstructure of UO_2 sample heated in temperature gradient furnace with top temperature 2600°C, bottom temperature 1150°C for 7 hrs. Magnification 20X.

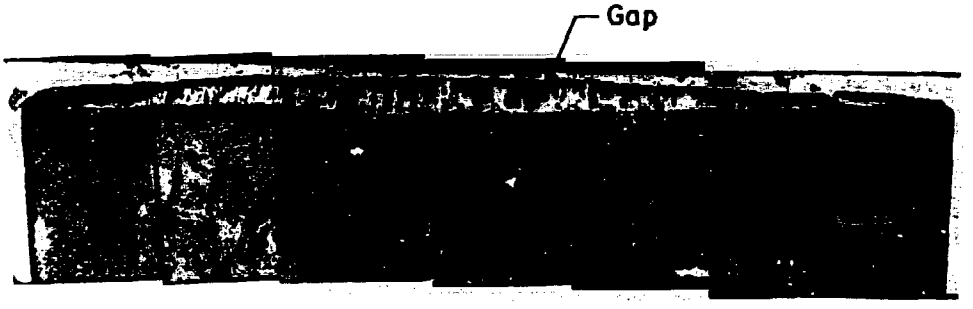

XBB 803-3779

Fig. 3-12. Cross section of top portion of UO_2 sample after temperature gradient heat treatment for 7.5 hrs. Highest temperature was 2600°C, the temperature gradient was ~1000°C/cm. The gap formed on top of UO_2 was filled with vapor-deposited crucible metal.

on the periphery near the tungsten crucible (Fig. 3-13). After numerous grinding/polishing operations, what we observed is shown schematically in Fig. 3-14. The inclusions are only found at hot end within 2 mm from tungsten crucible wall. We thought these inclusions might have migrated from the original plane of powders, because they were the same shape and size as the original tungsten spheres. We changed the temperature and duration of the experiment, in the hope of finding inclusions at places other than the periphery. We failed to see any inclusions that had migrated in the central part of the sample. After changing the inclusions from tungsten to molybdenum, we still saw inclusions only near the periphery of UO_2 sample. Microprobe and EDAX analysis showed these inclusions at the periphery to be tungsten, whether the original powder was molybdenum or tungsten. We realized that these inclusions were from the tungsten crucible and that they did not migrate from the original plane of powders. The inclusions near the tungsten crucible were formed by the following mechanism: At high temperature, tungsten from the crucible dissolved and diffused into UO_2 and precipitated out as inclusions during cooling down.

We tried to increase the temperature and the duration of the experiment, in the hope of inducing some migration, but without success. We could not increase the temperature of the crucible much more than 2800°C, because the crucible melted at local hot spots where the electron beam impringed.

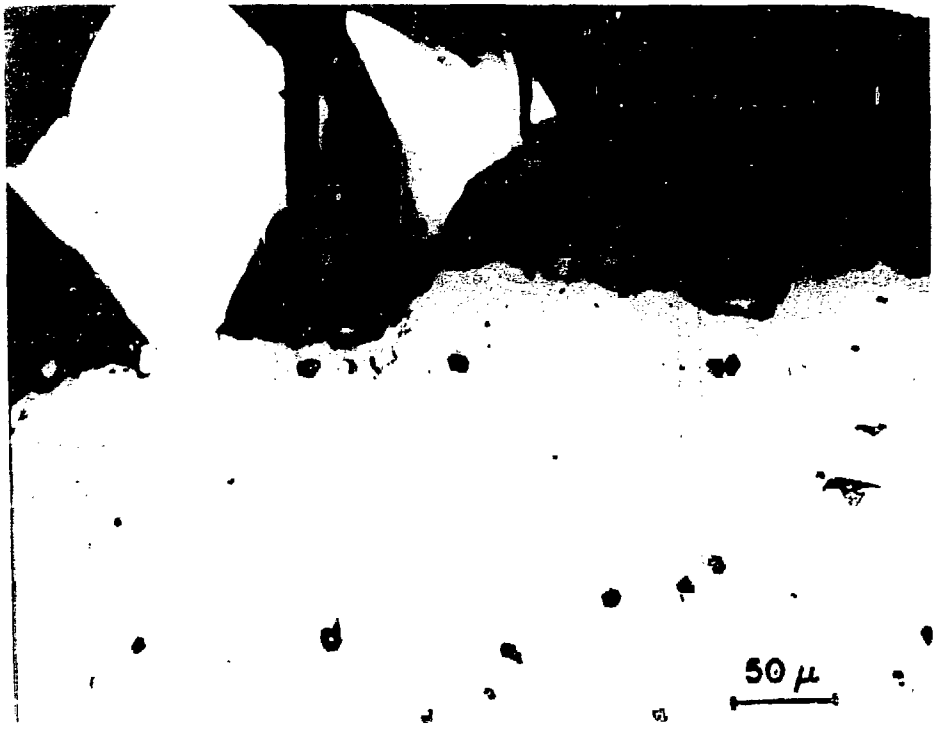

Fig. 3-13. Tungsten inclusions (white spherical dots) near the top corner of UO_2 sample (gray area). The big white chunk at top left is tungsten formed in the gap (black) by vapor deposition.

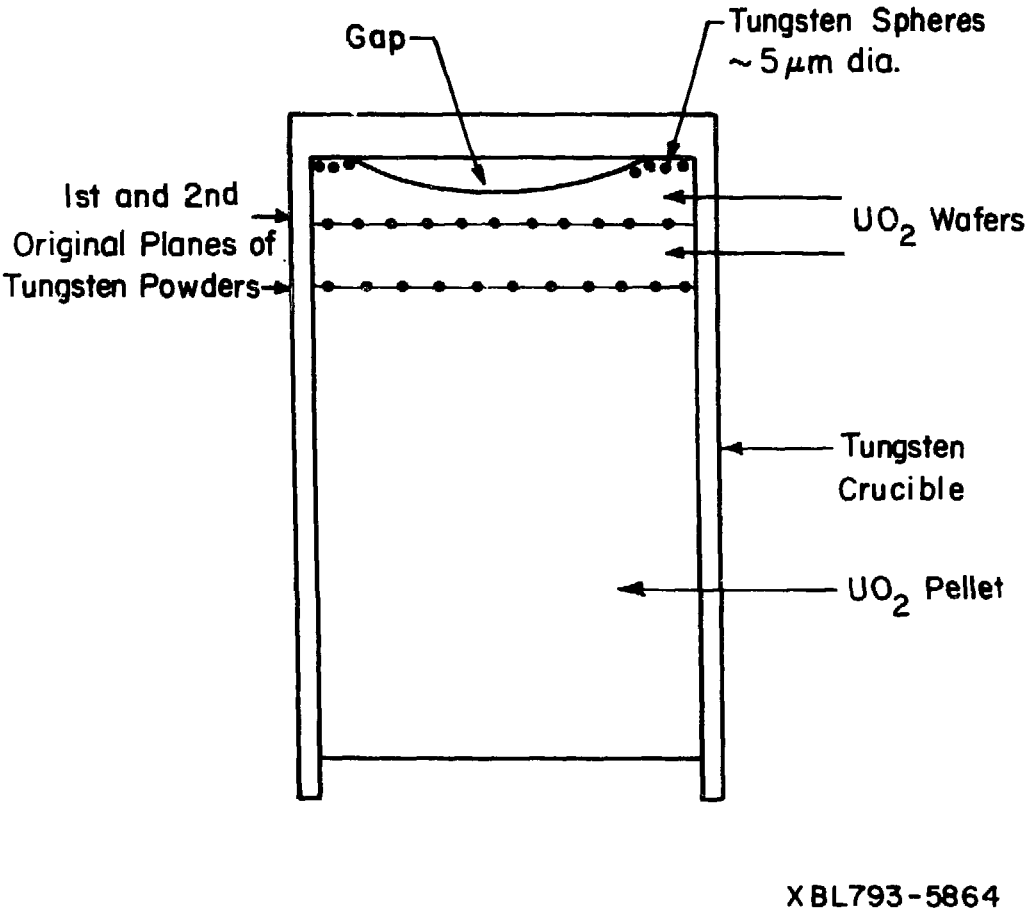

Fig. 3-14. Schematic diagram of UO_2 pellet-wafer assembly after thermal gradient migration experiment.

The only way to increase the temperature of the UO_2 sample was to eliminate the gap. Rough calculation showed that the presence of the gap lowers the temperature in UO_2 by more than 200°C (see Fig. 4-6).

C-2. Elimination of the Gap

The gap was formed due to: 1) The porosity in UO_2 sample and the residual cracks between the UO_2 wafer and pellet which migrated to the top under the influence of temperature gradient. 2) Vapor transport. Due to radiation loss from the periphery of the tungsten crucible, the central part of the sample is hotter than the periphery. UO_2 evaporated from the central part and deposited at the colder places, such as the periphery of UO_2 and the radial space between the UO_2 specimen and the tungsten crucible, thus leaving the central region depressed by as much as 0.7 mm. The gap destroys the physical integrity of the wafer, making it impossible to measure the migration distance in the central portion of the sample and lowers the temperature of the UO_2 sample, thereby significantly slowing down the migration rate of the inclusions. Several effort were made to eliminate the gap. These efforts were in two directions: (i) To reduce the porosity. (ii) To eliminate/reduce the radial temperature gradient.

(i) To Reduce the Porosity

(i)-a. Eliminate the radial space between UO_2 and the tungsten crucible. The crucible we used initially were made of a tungsten tube to which a tungsten lid was electron beam welded. The electron beam welding procedure distorted the tube slightly, thus requiring the use of tubes which were 0.025 cm larger than the sample. This left a large radial gap for vapor transport.

We thought that chemically vapor deposit tungsten on UO_2 sample would make a perfectly tight fitting curcible. However, we had difficulties depositing tungsten on UO_2 because WF_6 and HF attack the UO_2 surface. We could not deposit a good integral layer of tungsten on UO_2. We finally sent one sample to Los Alamos National Laboratory to be coated. Their approach to the problem was to sputter a thin film of tungsten ($\sim$200 Å) on UO_2, then deposit a thick layer ($\sim$0.038 cm) of tungsten by chemical vapor deposition. However, when heating up the sample in thermal gradient experiment, the tungsten layer blistered and broke. The tungsten "crucible" created this way was just not strong enough for the purpose. Our solution to this problem was to order an integral CVD tungsten crucible (i.e., tube plus lid) which permit a close fit to UO_2 specimen, instead of using crucibles which were made by welding a lid to a tube. The radial gap was reduced to $\sim$30 μm by the new arrangement.

(i)-b. Premelt UO_2 to eliminate porosity. Polycrystalline UO_2 pellets were placed in a tungsten crucible and heated in vacuum to 1000°C for 2 hrs to eliminate adsorbed moisture. Then a tantalum plug was E.B. welded onto the crucible in vacuum. The whole crucible was then hung in a tungsten resistance furnace and heated to 2900°C. After burning out a couple of tungsten mesh heating elements (which were designed to operate at 2600°C), we did manage to melt UO_2 and get very high density UO_2. We removed the melted UO_2 from the tungsten crucible by dissolving the crucible in a mixture of H_2SO_4 and HF. However, the UO_2 was not porosity-free and was too brittle to be used in temperature gradient experiments.

(i)-c. Reduce porosity by applying a temperature gradient to the sample. From previous experience, we knew that porosity and voids migrate to the high temperature side under the influence of temperature gradient. By heating UO_2 several times in a temperature gradient furnace, like the one in Fig. 3-8, we hoped to eliminate the voids. We found that the porosity could not be completely eliminated by repeated thermal gradient treatment. After several heat treatment, the UO_2 sample became very fragile, but was still full of pores and voids.

(i)-d. Isothermal sintering with a yoke. As described in section B-1, the isothermal sintering of UO_2 sample in a yoke increased the grain size, densified the sample, eliminated the gap at the inclusion between the wafer and pellet. However, porosity in the bulk was not substantially reduced by this procedure, although the pellet/wafer gap was closed (see Fig. 3-7).

(ii) Eliminate/Reduce the Radial Temperature Gradient

(ii)-a. Put a piece of iridium between UO_2 and tungsten lid. The concept here is that even if a gap formed, iridium would melt and filled the gap. Therefore, the temperature in UO_2 would not be lowered significantly at the center. However, iridium reacted with tantalum and tungsten crucible and formed a low melting eutectic[46,47] which destroyed the crucible.

(ii)-b. Preferential heating on the periphery. We tried to achieve more uniform radial temperature distribution by heating more on the periphery of tungsten lid than on the center. The approaches are: 1. E.B. heating only the periphery of the lid. 2. Making a shoulder on the tungsten crucible as shown in Fig. 3-15a. The edge is closer to the filament than the center and

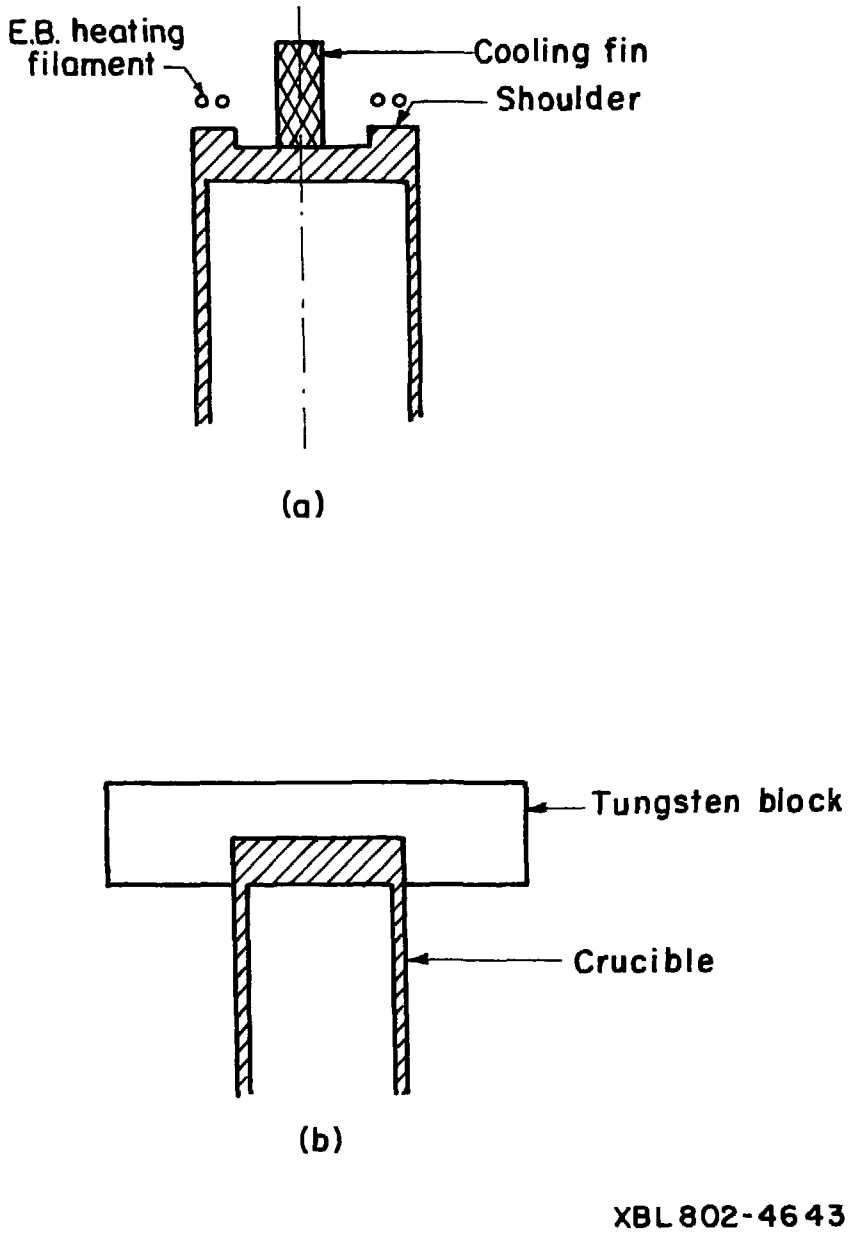

Fig. 3-15. Various shapes of crucibles designed for peripheral heating.

therefore attracts more electrons. In addition, a cooling fin (Fig. 3-15a) is placed in the top center of the crucible to dissipate heat. We placed a large tungsten block on top of the crucible as shown in Fig. 3-15b. The radial temperature gradient of any cylinder is largest near the periphery due to radiation heat loss. By using a tungsten block much larger than the crucible, we hoped to achieve a more uniform radial temperature distribution in the crucible. However, the tungsten block was too massive and not enough power was available to heat the UO_2 to high enough temperature to check if this approach would work or not. But calculation (see Chapter 4) shows that even if this approach gives uniform temperature at top UO_2-crucible interface, the radiation loss from side of crucible would still create significant radial temperature gradients in the UO_2 sample.

(ii)-c. Thick-walled tungsten crucible. We changed the wall thickness from 0.038 cm to 0.114 cm, so that more heat was conducted down the wall. This would bring up the temperature of UO_2 along the periphery and reduce the radial temperature difference in the UO_2.

(ii)-d. A thermal shield was placed around the tungsten lid to cut down the radiation heat loss from side of crucible.

Although some of the efforts mentioned were not successful, the lessons we learned helped us design a better temperature gradient furnace. By a combination of using presintered pellet-wafer specimens in an integral thick-walled tungsten crucible, concentrating E.B. heating on the periphery of the top lid and placing a thermal shield around the lid, the concave gap was reduced to about 10% of its original size (i.e., to a maximum depth of ~0.1 mm).

C-3. Thermal Gradient Annealing of Tungsten and Molybdenum Inclusions

After the concave gap was eliminated, several thermal gradient experiments were performed. Spherical molybdenum and tungsten powders 1-5 μm diameter were used as inclusions. The top temperature at black body hole was between 2400°C and 2700°C. The bottom temperature of UO_2 was about 1200°C. Each sample was held at temperature for about 12 hrs during each heat treatment. The sample was cut longitudinally, mounted, polished and examined, using the optical microscope, for the extent of migration of the inclusions. In most cases, we did not see any movement of these inclusions to either side of the original plane. Occasionally, we would observe some small movement of the inclusions (Fig. 3-16). Most of them moved toward the hot side but sometimes we observed some inclusions on the cold side of the original plane. We increased the temperature to 2800°C and the duration of the thermal gradient heat treatment to 36 hrs, however, the number of inclusions displaced from the initial plane and the distance they had migrated was still very small. The largest distance observed was less than 200 μm. According to surface diffusion theory, for a 5 μm tungsten inclusion in UO_2, a temperature at UO_2 wafer-pellet interface of 2500°C, and a temperature gradient of 1300°C/cm, the displacement would be 800 μm in 12 hrs (see Appendix A). In calculating the velocity of tungsten inclusion, we used the surface diffusion coefficient and the activation energy of uranium dioxide, whereas our experiment involves the interfacial diffusion of UO_2 molecules around tungsten inclusions. The interfacial diffusion mechanism between UO_2 and tungsten apparently is very different from the surface diffusion of uranium oxide, but there

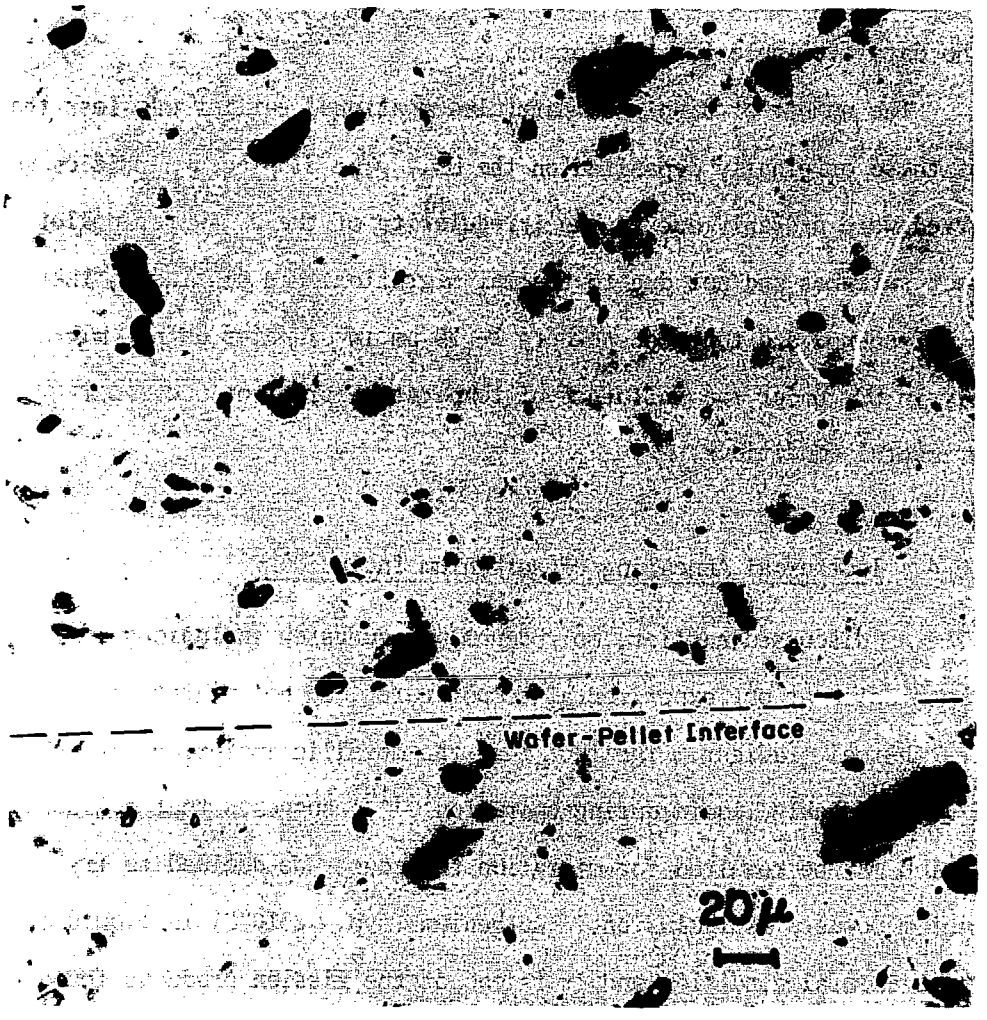

XBB 806-7282

Fig. 3-16. Inclusions away from original plane. Annealed at top sample temperature of 2500°C, bottom temperature of 1100°C, for 8 hrs.

are no data available for the former.

The number of displaced particles mentioned earlier was less than 5% of those originally deposited on the UO_2. The displaced particles we observed were probably due to the irregularity of the UO_2 wafer-pellet contact surfaces and not due to thermal migration. We concluded, therefore, that molybdenum and tungsten powders 1 - 10 μm in diameter do not migrate bodily in UO_2 under the influence of temperature gradient under our experimental conditions.

C-4. Isothermal Annealing of Ruthenium Inclusions

As discussed earlier, molybdenum and tungsten inclusions, which are both solid at our experimental temperatures, do not migrate bodily in the thermal gradient. The fact that the metallic inclusions in reactor fuel were probably liquid during operation[7,10] suggests that a liquid inclusion may be required for migration to occur. We decided to try ruthenium powders as inclusions. Ruthenium (m.p. = 2310°C) is liquid at our experimental condition and it is one of the fission products found in metallic inclusions in reactor fuel.

Before each thermal gradient experiment, we sintered each sample isothermally as described in section B-1 of this chapter. After isothermal annealing of the ruthenium inclusions (~1 - 10 μm in size) in UO_2 at 2250°C for 30 hrs, we found (unexpectedly) that the ruthenium had diffused into UO_2 matrix. As shown in Fig. 3-17, the grain boundaries are seen to be decorated with a metallic phase (white). Electron microprobe analysis showed that the metallic phase contained uranium and ruthenium. No

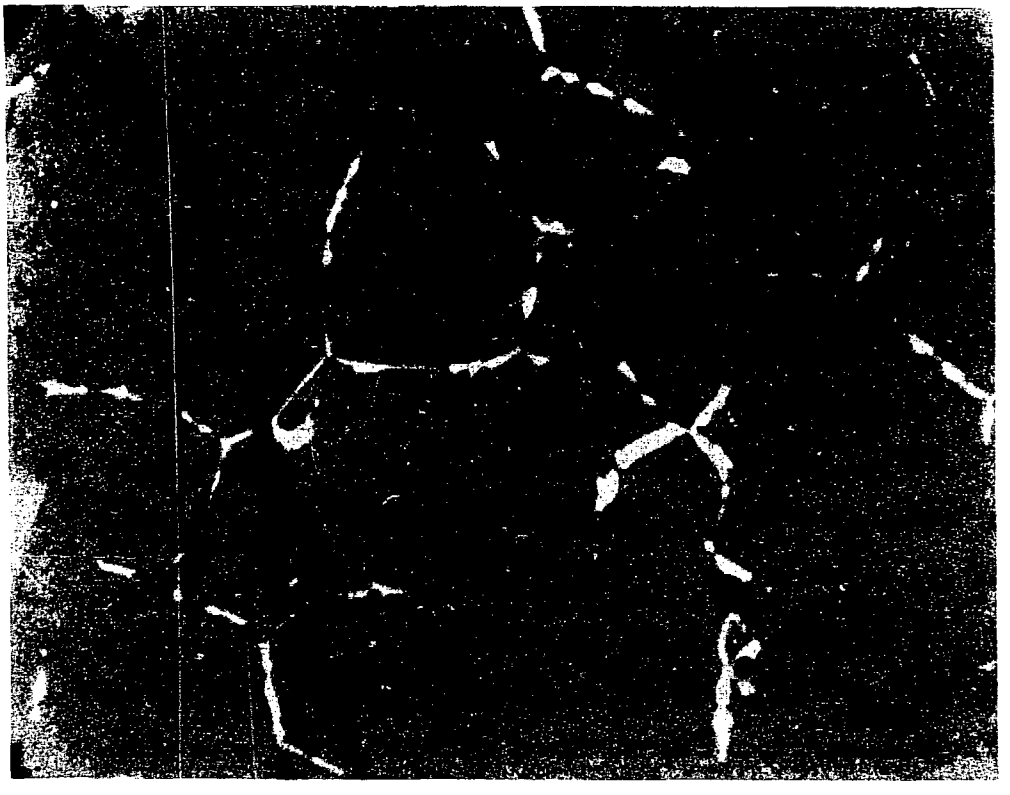

XBB 806-7283

Fig. 3-17. Ruthenium on grain boundaries of UO_2 about 350 μm away from the original interface after annealing at 2250°C for 30 hrs.

detectable amount of ruthenium was found in the UO_2 grains.

An additional experiment was conducted to determine whether the ruthenium inclusions migrated as entities or whether the mechanism was one of solution of ruthenium in UO_2 followed by diffusion in atomic form. To clarify this point, the ruthenium powders were replaced by a ruthenium disk (~0.076 cm thick). After a high temperature anneal, essentially the same type of ruthenium migration pattern as shown in Fig. 3-17 was observed. Since the ruthenium disk could not break up into small particles, ruthenium dissolved into UO_2 and migrated as atoms.

In order to determine whether the diffusion process occurred via grain boundaries or in the UO_2 crystal lattice, ruthenium powders were placed between two UO_2 single crystal wafers and the assembly was annealed isothermally. Post-anneal microscopy (Fig. 3-18) revealed that essentially no ruthenium had penetrated the UO_2 single crystal. This experiment demonstrated that the dissolution and diffusion process occurred through the grain boundaries of UO_2.

To study this diffusion phenomena quantitatively, we performed the isothermal anneals of ruthenium powders between UO_2 pellets at different temperatures in the apparatus shown in Fig. 3-5 and Fig. 3-6. The flowing gas mixture was 4% H_2 and 96% Ar. The alignment tube and separators used were made of either molybdenum or tungsten. After each experiment, the sample was mounted, and approximately 50 μm thick layers were ground off (parallel to the original ruthenium plane) at a time. After each grinding, the ruthenium-to-uranium ratio on the exposed surface was determined by x-ray fluorescence. By repeating this grinding and counting procedure, we obtained the diffusion profile of ruthenium

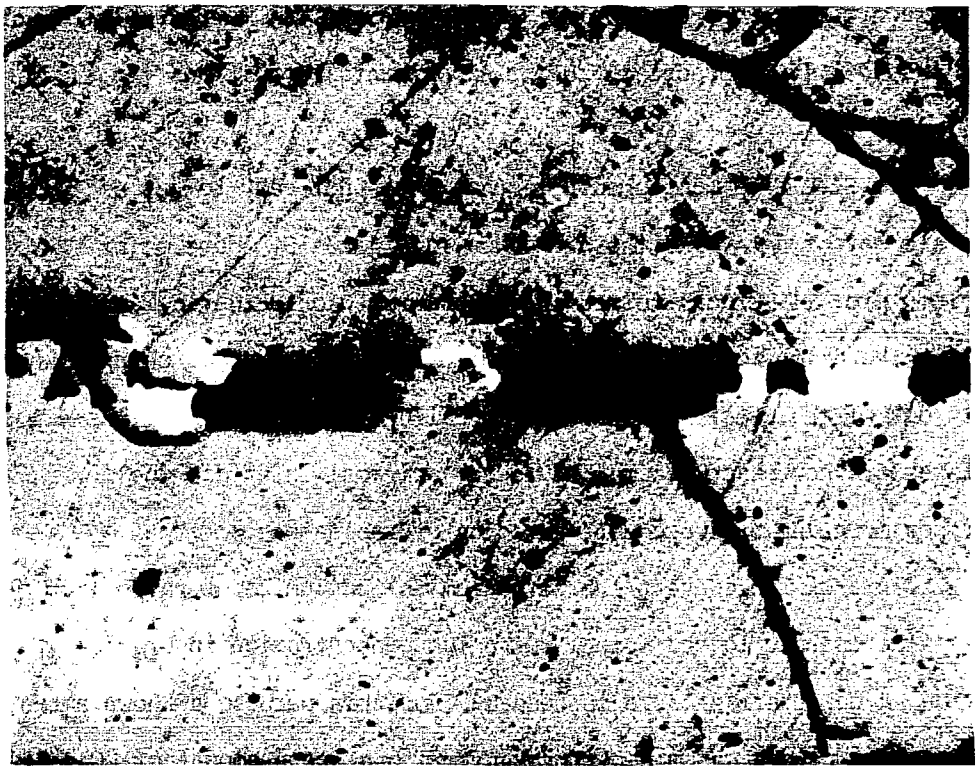

XBB 803-3781

Fig. 3-18. Annealing of ruthenium (white) in single crystal UO_2 at 2250°C for 12 hrs.

in UO_2. A typical distribution is shown in Fig. 3-19, in which the solid line drawn through the data points shows the best fit to the solution of Fick's second law appropriate to our experimental conditions [Eq. (12) of Chapter 2].

It should be mentioned here that it is not easy to get a complete set of data like the one shown in Fig. 3-19. Some major problems are: 1. Cracks formed in the uranium dioxide during annealing destroy the diffusion profile; 2. Samples became broken or chipped when taken out of the crucible after the annealing experiments; 3. The exposed surfaces are not exactly parallel to the original interface due to improper mounting or subsequent grinding of the sample.

In order to convert the ruthenium-to-uranium count ratio from x-ray fluorescence to the actual ruthenium concentration in uranium dioxide, a calibration curve is needed. For this purpose a known amount of ruthenium powder was mixed thoroughly with a known amount of UO_2. The mixture of powders were then pressed to form a pellet of the same configuration as the annealed sample and analyzed by x-ray fluorescence. Repeating this process several times with different proportions of ruthenium and uranium dioxide, we obtained the calibration curve shown in Fig. 3-20. This curve permits conversion of the Ru/U count rate ratio to the actual concentration of ruthenium in uranium dioxide.

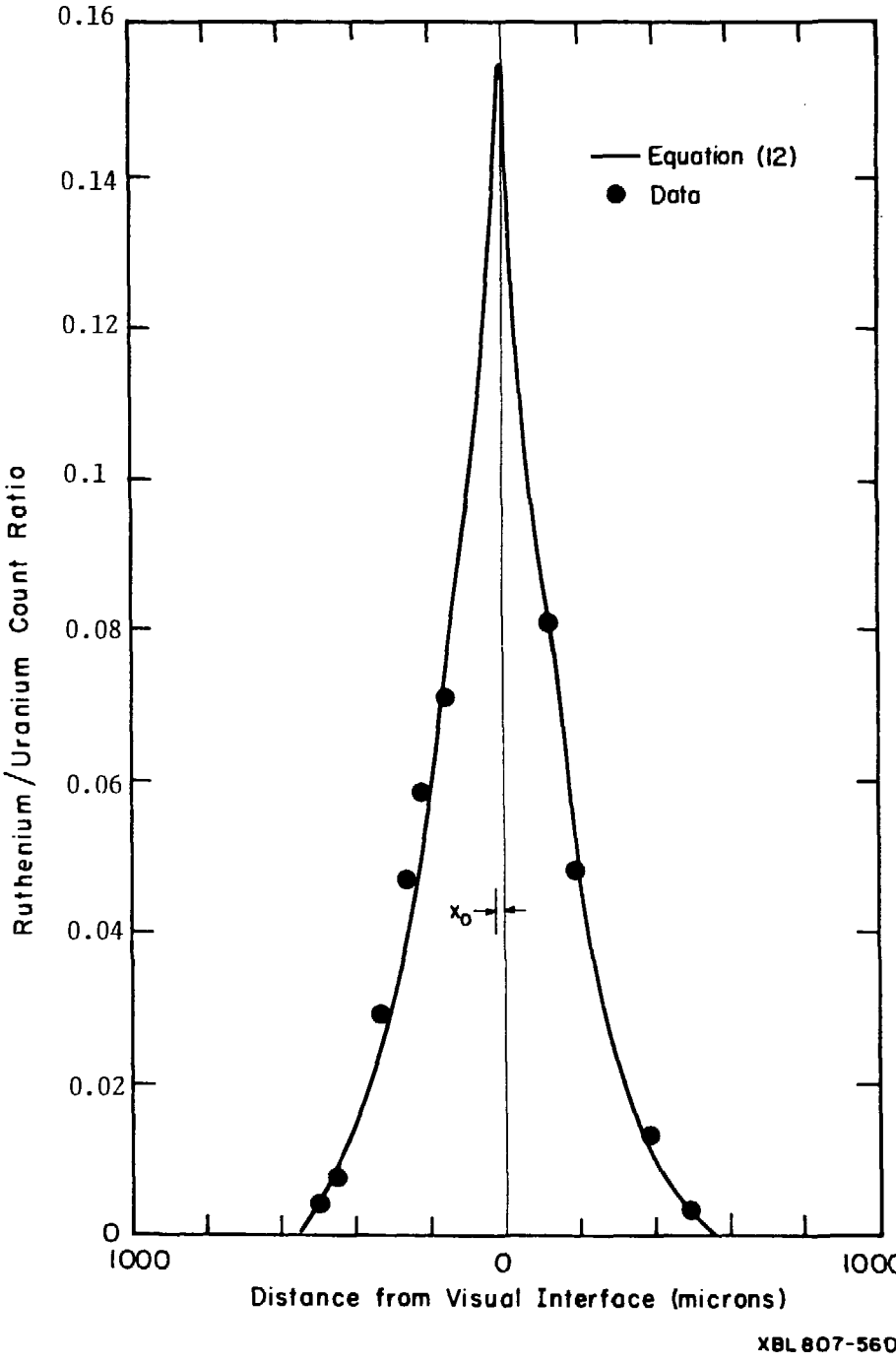

Fig. 3-19. Isothermal diffusion profile of ruthenium in UO_2. (Sample 9-12-2.)

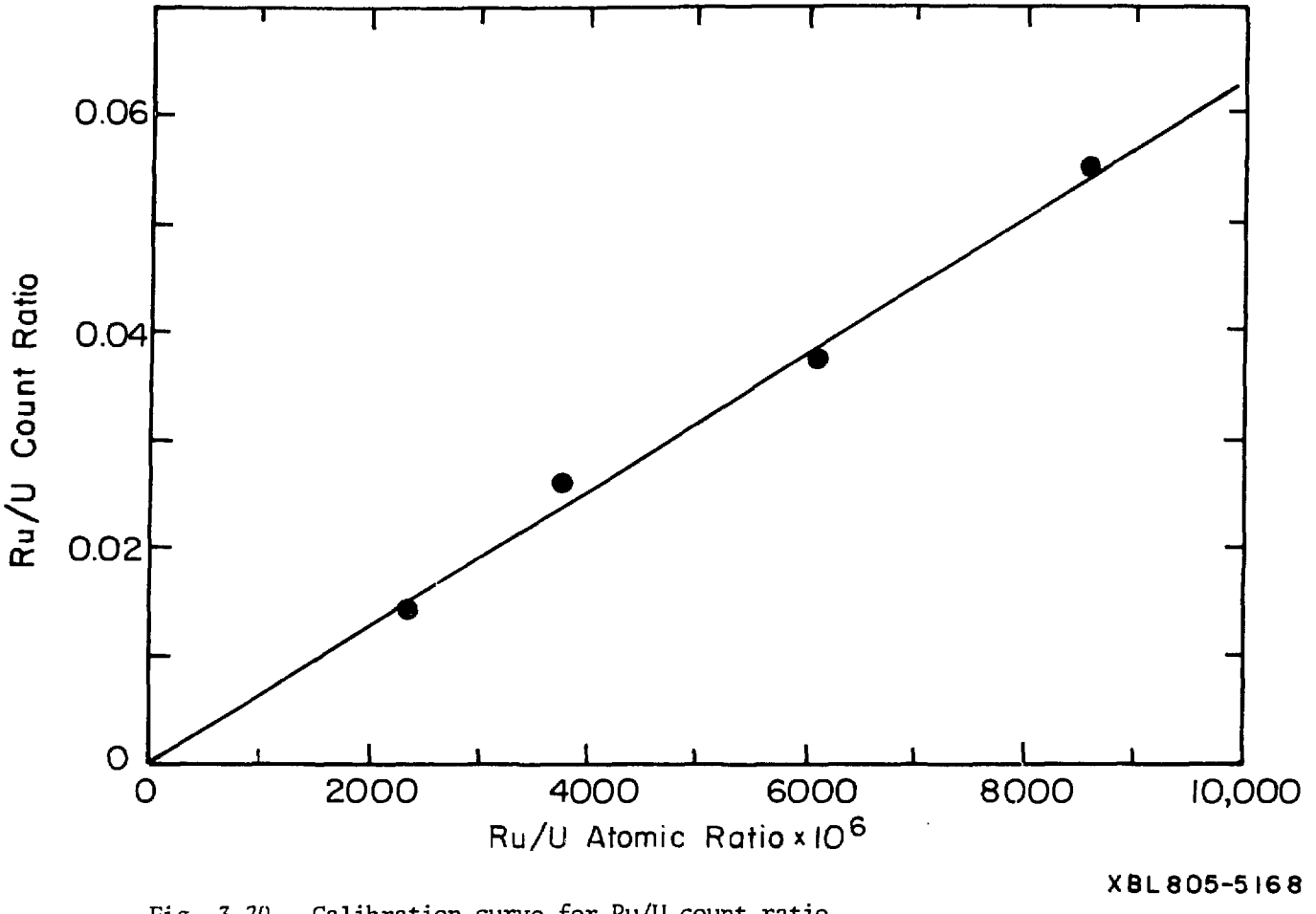

Fig. 3-20. Calibration curve for Ru/U count ratio.

C-5. Temperature Gradient Annealing of Ruthenium Inclusions

In order to determine whether the transport of ruthenium in uranium dioxide under the influence of temperature gradient was influenced by a true Soret effect, we performed several temperature gradient anneals of ruthenium powders in uranium oxide using the temperature gradient furnace shown in Fig. 3-8. The same experimental procedure was employed as described in section C-3, except that ruthenium was used in place of tungsten powders and no preliminary isothermal annealing was employed. The temperature gradient annealings lasted between 12 hrs to 36 hrs. After the heat treatment, the top lid of the tungsten crucible was cut off carefully with a diamond saw, then the tungsten crucible was slotted longitudinally at several places. We then broke the crucible to remove the sample. The sample was then mounted and counted the same way as described in section C-4 to obtain the diffusion profile. In these experiments, ruthenium usually concentrated in the central portion of UO_2 rather than spreading axially uniformly over the entire radius as in the isothermal annealing experiments. This phenomena was probably caused by the temperature gradient in radial direction. A typical axial diffusion profile of ruthenium in temperature gradient annealing is shown in Fig. 3-21. The radial nonuniformity of the Ru/U ratio is averaged by the large detection area of the x-ray fluorescence spectrometer.

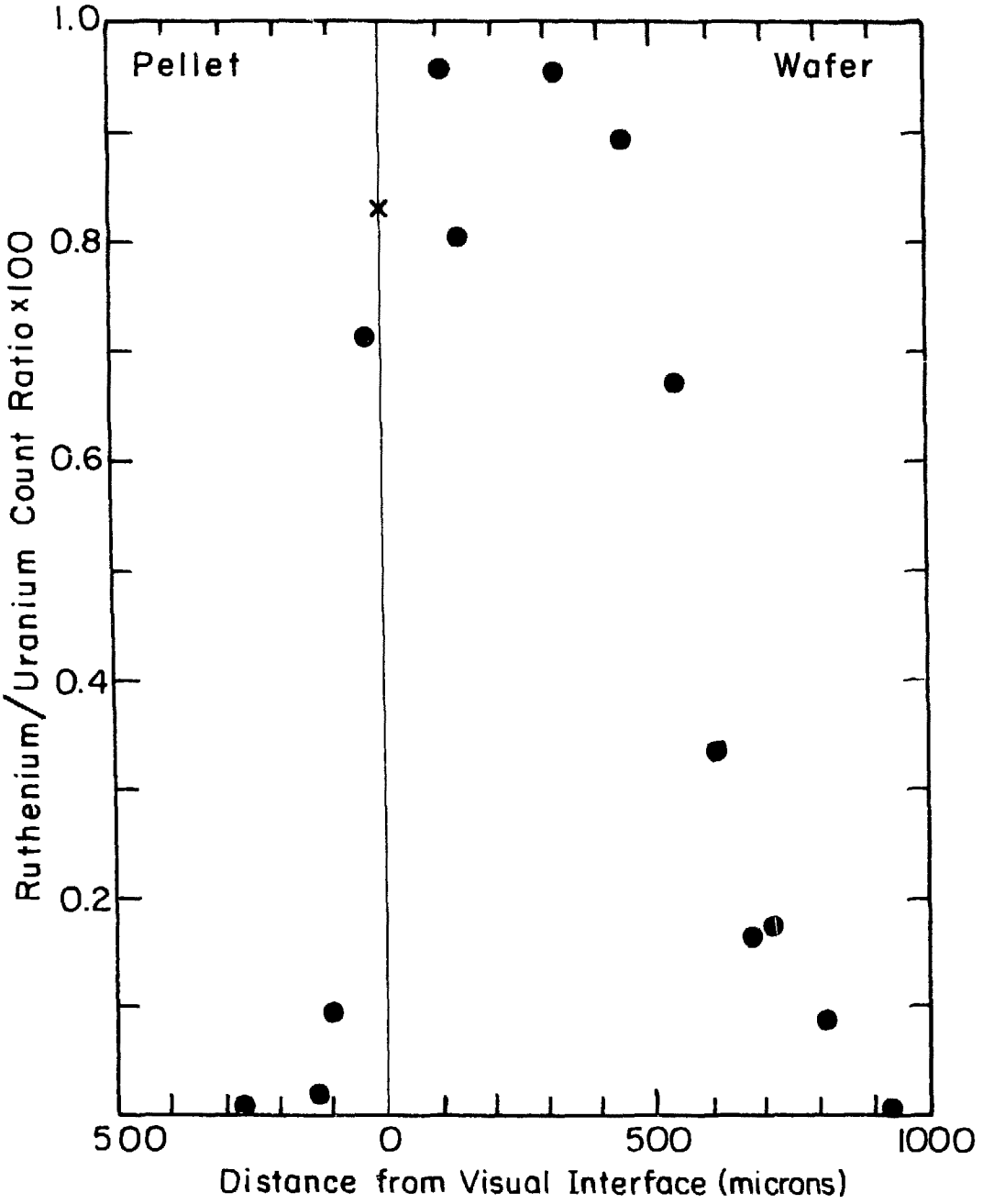

XBL 807-5600

Fig. 3-21. Diffusion profile of ruthenium in UO_2 under the influence of temperature gradient for 35 hrs. The temperature distribution of the sample is shown in Figs. 4-3 and 4-4. x indicates the solubility at calculated interface temperature. (2261°C)

IV. TEMPERATURE CALCULATION

Since the diffusion process is temperature dependent, it is important to know the temperature distribution in the UO_2 sample. We calculated the temperature distribution in UO_2 under two conditions: (i) Assuming good conduct between UO_2 and the tungsten crucible on all sides (Fig. 4-1). (ii) Allowing for a gap (as discussed in section C-2 of chapter 3) between top of UO_2 and the tungsten (Fig. 4-2), calculation of the temperature distribution in the sample requires numerical solution of the steady state heat conduction equation in cylindrical coordinates with radiation heat transfer boundary conditions. We used the computer code HEATING 5[49], developed by Oak Ridge National Laboratory, to solve this problem. In this code, the thermal conductivity, density and specific heat can be both spatially and temperature dependent.

The calculation procedure is as follows: We first divide the sample and the crucible into different zones (six in Fig. 4-1 and nine in Fig. 4-2). Besides taking into account different materials (UO_2, tungsten and gap) and different boundary conditions, the zones are chosen is such a way that the decisive regions (e.g., region 3 in Fig. 4-1) and the relatively unimportant regions (e.g., region 5 in Fig. 4-1) are in different zones. This enables us to use a finer mesh in the critical regions so the temperature could be more accurately calculated here. After the zones are chosen, a network of lattice lines, equally

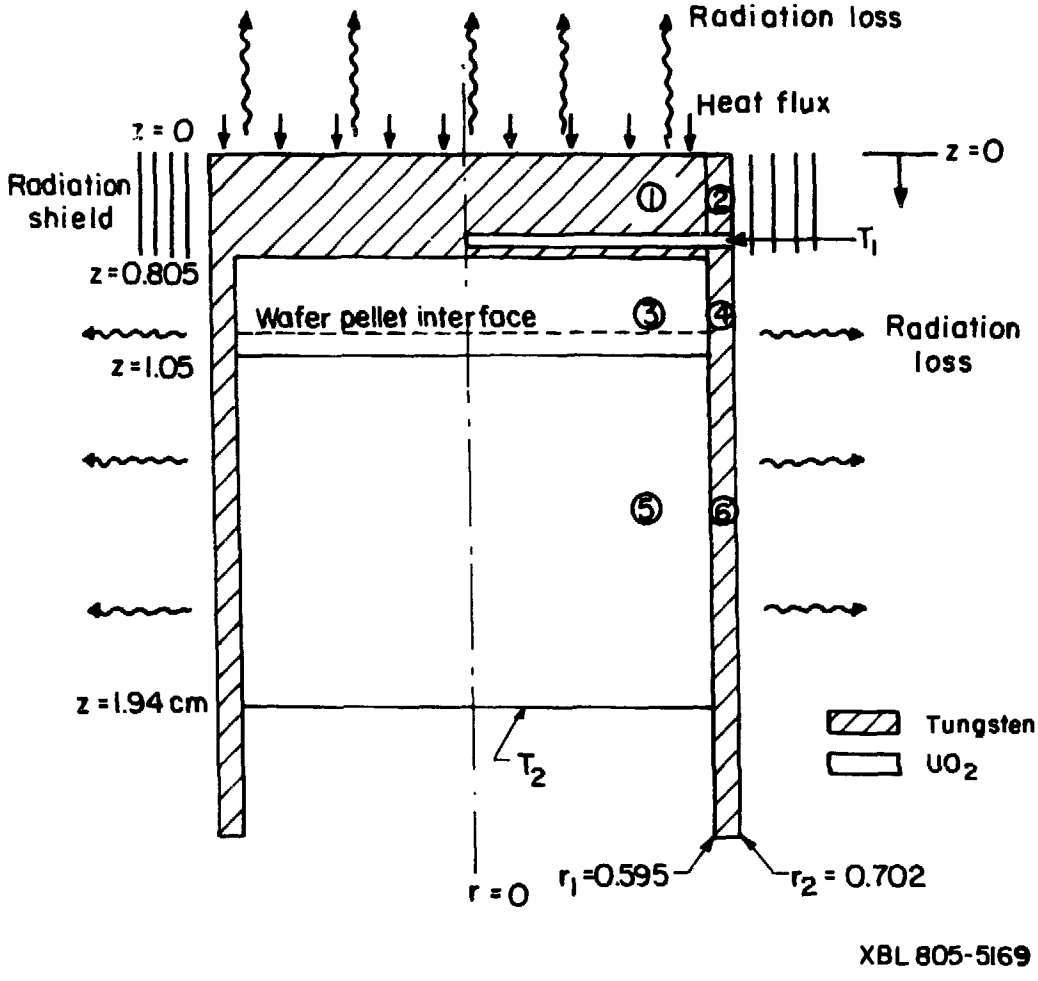

Fig. 4-1. Cross section of specimen in the thick-wall crucible. UO_2 in good contact with crucible on all sides (all dimensions in cm).

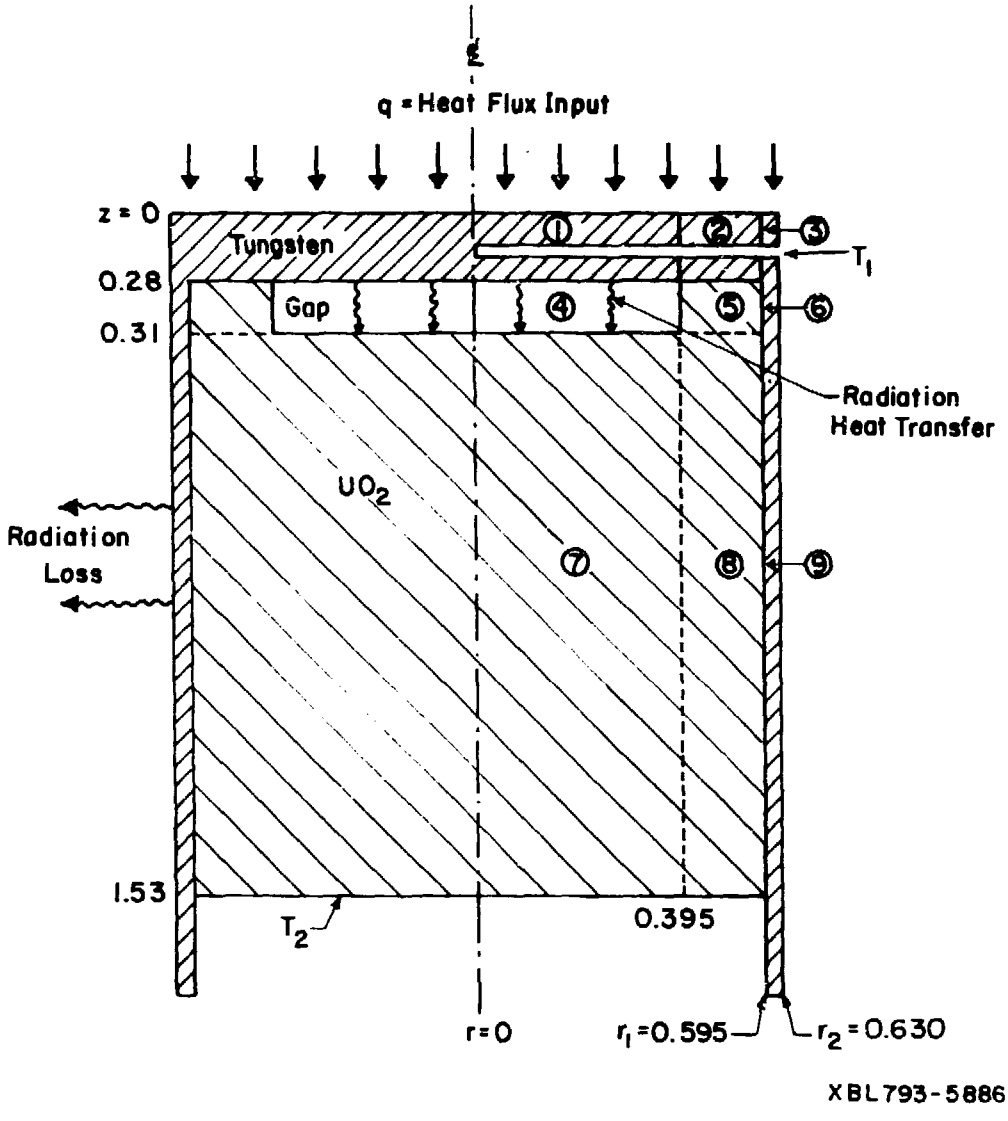

Fig. 4-2. Cross section of the specimen in the thin wall crucible when there is a gap, (all dimensions in cm).

spaced in each zone and parallel to the r and z directions, is laid across the specimen. The intersections of the lines are called nodes. The heat conduction equation is then replaced by a system of finite difference heat balance equations at each node. Boundary conditions must be specified on the exterior boundaries of each zone.

We have the two measured temperatures (T_1 and T_2) and the heat flux q from electron beam power supply to serve as the basis for calculating the temperature distribution. The temperature T_1 is the temperature at the axial position of the black body hole measured by focusing the optical pyrometer on the bottom of the black body hole (r = 0). All the necessary corrections for absorption and non-black body conditions are accounted for. Due to the presence of the thermal shield around the tungsten lid, the lid is assumed to be adiabatic in the radial direction. The temperature drop from the center of the tungsten lid (r = 0) to the surface of the lid ($r = r_2$) is usually calculated to be less than 50°C.

The temperature T_2 is assumed to be constant over the entire bottom surface of UO_2. The tantalum partial ring (11 in Fig. 3-8) was included to achieve constant temperature here. However, there is considerable conduction from the tungsten wall to the UO_2, so the temperature is probably not constant over the entire bottom surface of UO_2. Fortunately, we are most interested in temperature at the hot end, and the errors introduced at the cold end do not significantly affect the temperature distribution at the hot end.

The thermal conductivity of tungsten is assumed to be constant

at 1 W/cm°K[50] in this temperature range. The thermal conductivity of UO_2 is allowed to vary with temperature.[51] There is radiation loss from the top of tungsten lid and the side of tungsten crucible (except for the tungsten lid).

An estimated heat flux, q', is used for a preliminary temperature calculation. The calculated temperature at the black body hole (r = 0) was compared with the experimental value T_1. The input flux is adjusted and the calculation repeated until the calculated temperature at the black body hole and the experimental value T_1 are the same. Usually the input heat flux in the calculation agreed with the experimentally measured heat flux (the power output from the electron beam power supply divided by the area of the top of the crucible) to within 15%. The resultant radial temperature distributions in a UO_2 specimen with and without a gap are shown in Figs. 4-3 and 4-5 respectively. The axial temperature distribution along the axis (at r = 0) of the sample are shown in Figs. 4-4 and 4-6.

In Figs. 4-3 and 4-4, the temperature distributions in the sample were calculated with and without radiation shields around the lid of the crucible. Both plots correspond to the same temperature at the black body hole. The radiation shield around the tungsten lid reduces the input power and the radial temperature gradient.

The accuracy of this calculation depends on the validity of the assumption that the UO_2 specimen is in good thermal contact with the tungsten crucible at all points. This should be a very good assumption along the side wall, because UO_2 expands much more than the tungsten

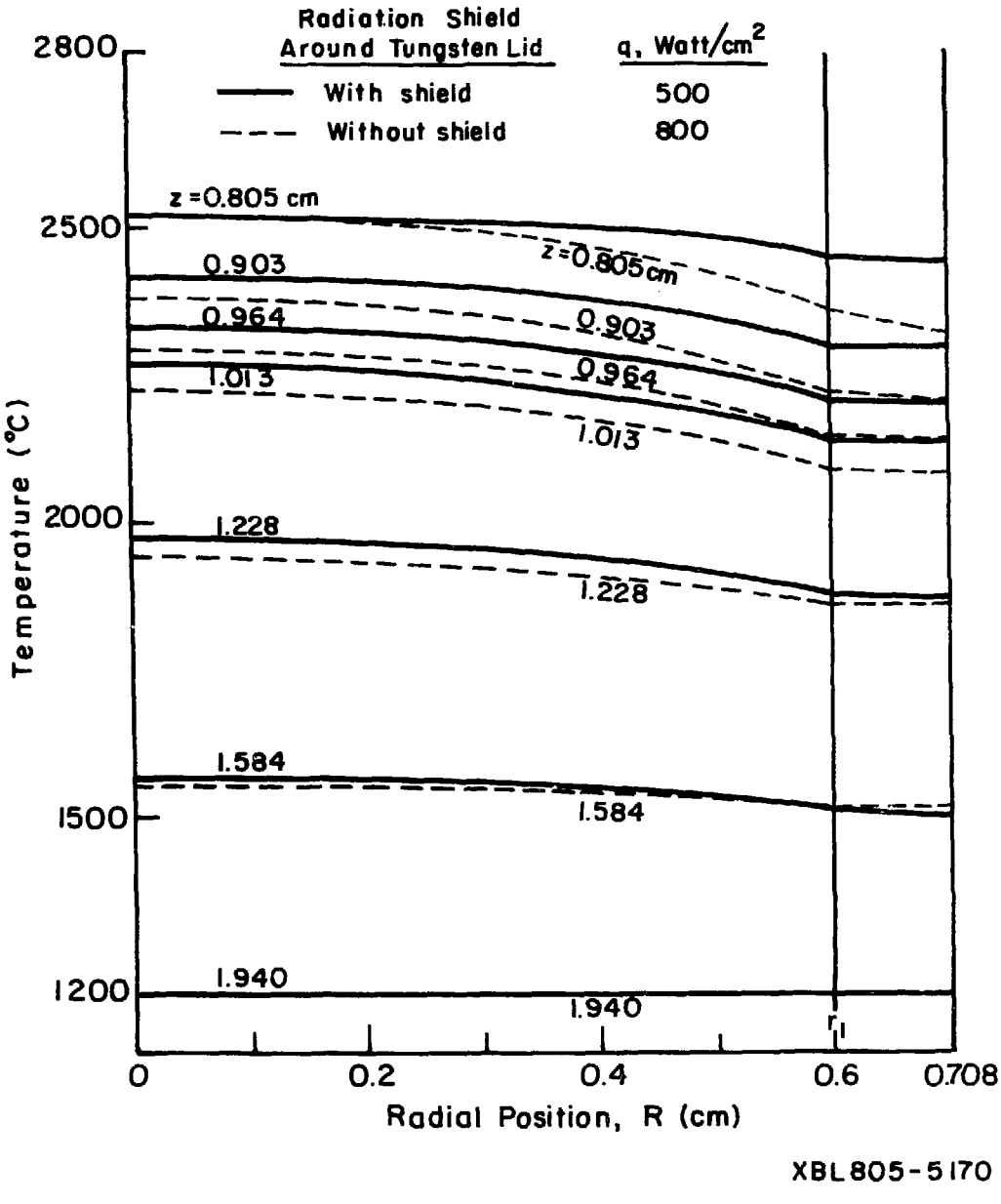

Fig. 4-3. Radial temperature distribution in UO_2, without a gap. (T_1 = 2550°C, T_2 = 1200°C, geometry shown in Fig. 4-1.)

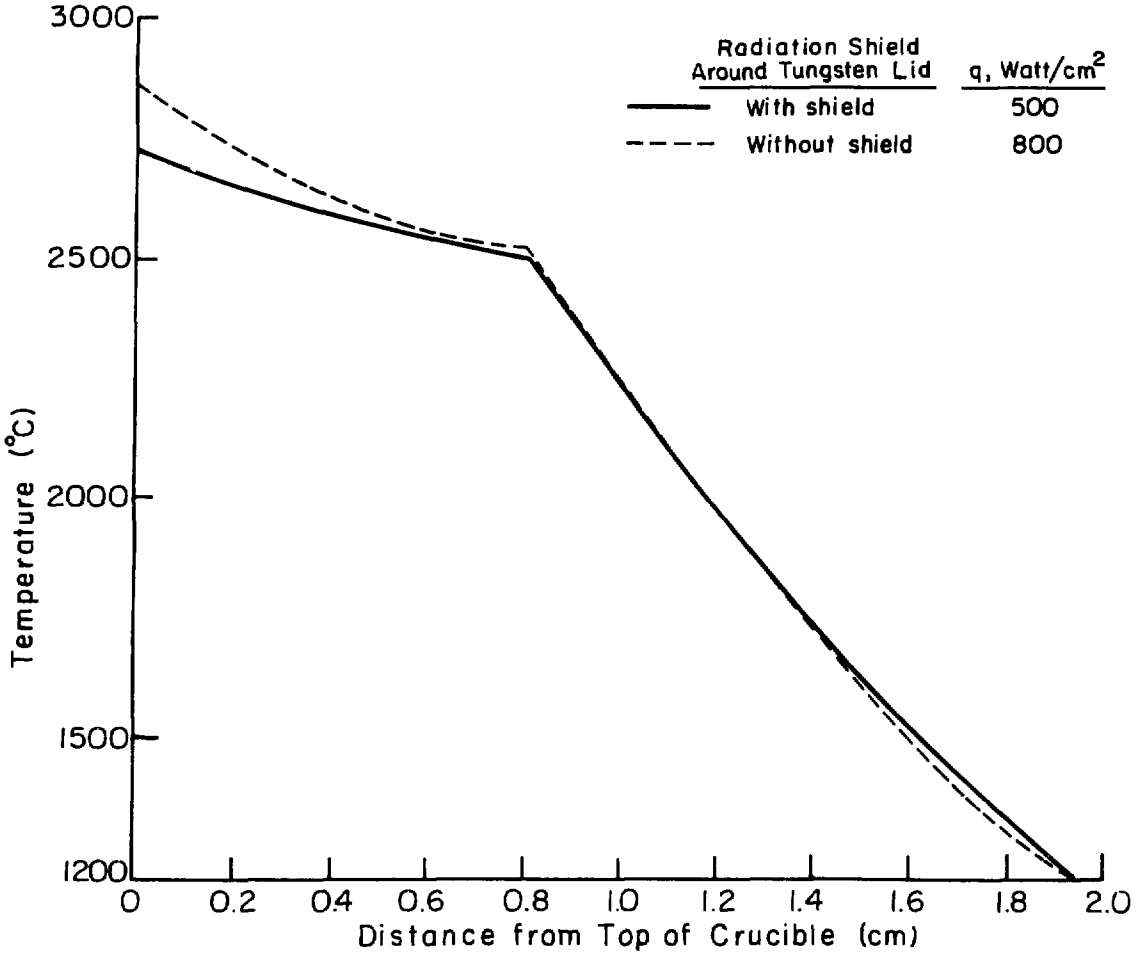

Fig. 4-4. Axial temperature distribution at center of crucible (r = 0). Same condition as Fig. 4-3.

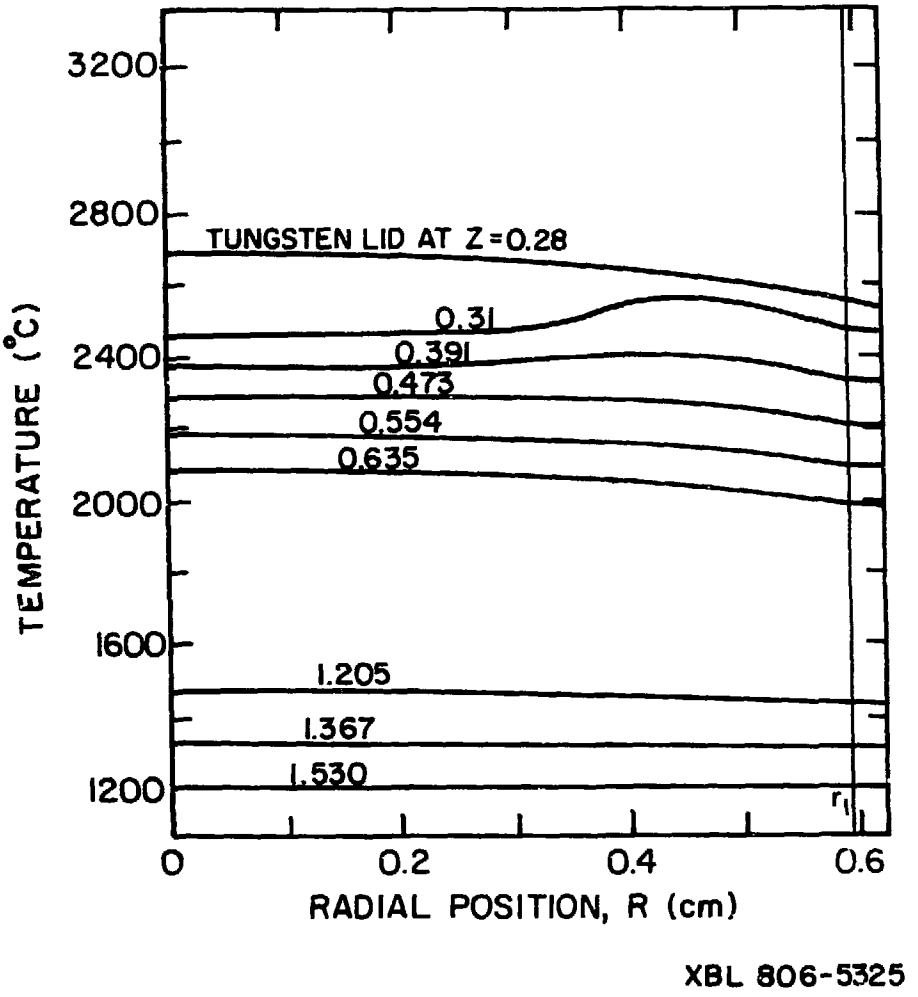

Fig. 4-5. Radial temperature distribution in a sample shown in Fig. 4-2, with T_1 = 2690°C, T_2 = 1200°C, and q = 450 watt/cm^2, and no radiation shield. (Temperature distribution with a gap.)

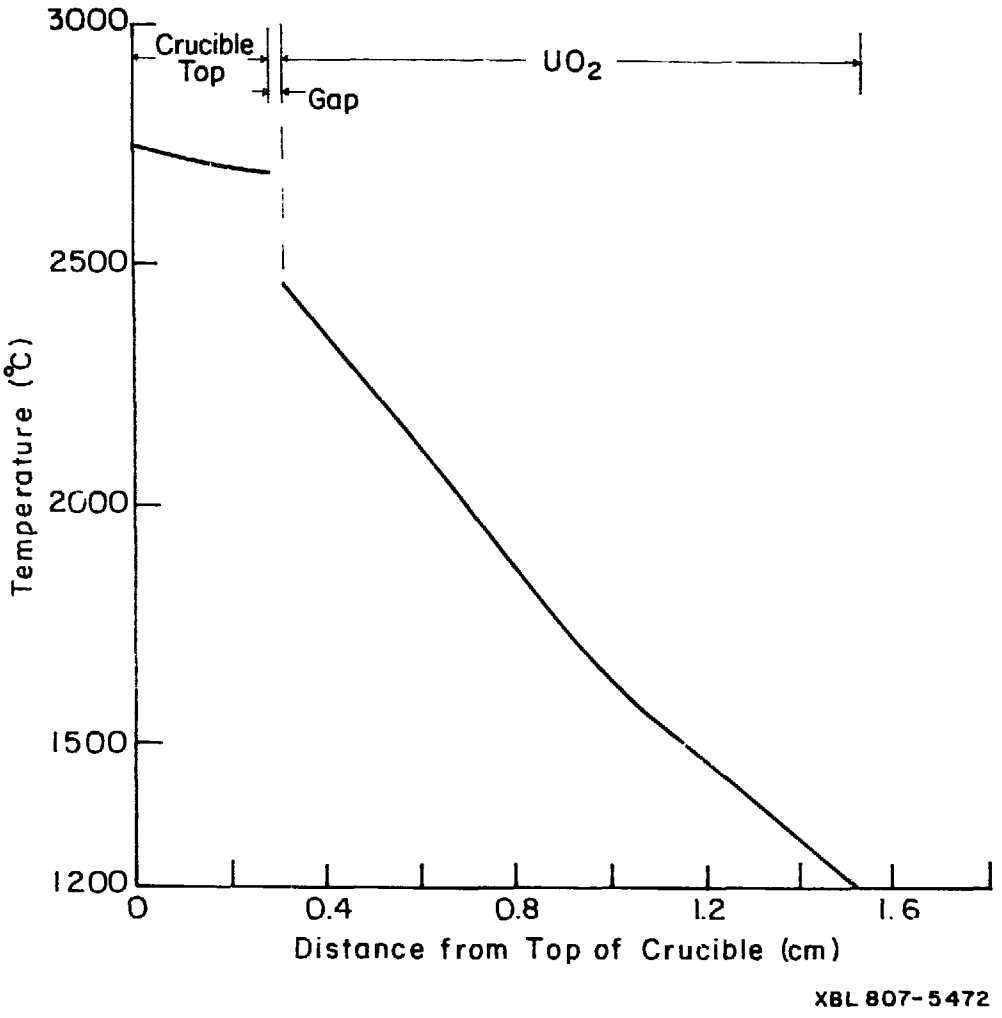

Fig. 4-6. Axial temperature distribution of the sample at r = 0, when there is a gap (configuration and radial temperature distribution shown in Figs. 4-2 and 4-5, respectively).

container and the initial radial gap closes at operating conditions. In addition, any radial gap between the specimen and the tungsten crucible would have been closed by vapor transport of UO_2 at this high temperature after a short heating period. The contact between the top of specimen and the crucible lid, however, is not as good, and a gap is formed in the central region by migration of void volume to the hot part of the system and transportation of UO_2 vapor from the hot to the colder area. The vapor transport mechanism at the top of the UO_2 sample provides good contact with the tungsten lid near the periphery and leaves a gap in the central region, as demonstrated in Figs. 3-11 and 3-14.

For the convenience of calculation, the concave gap is approximated by a disk of constant thickness (0.3 mm in Fig. 4-5) with a diameter of 0.79 cm, which is less than the diameter of the UO_2 sample. The top of the UO_2 is in contact with tungsten lid along an outer region ~0.2 cm wide (region 5 in Fig. 4-2). The dimension of the gap (region 4 in Fig. 4-2) is chosen so that it is equal to the volume of a typical concave gap observed (0.7 mm). After the thermal gradient experiment, the volume of the concave gap was roughly estimated from the profile of the gap traced out by a profilometer. In the calculation, it is assumed that thermal radiation contributes to most of the heat transfer in the gap. This assumption is valid because the contribution from the conduction of the g n the gap is small compared to radiation heat transfer at such high temperatures. As shown in Figs. 4-5 and 4-6, for a fixed temperature T_1 at the black body hole, the presence of the gap would reduce the temperature in the UO_2 sample by as much as 230°C. In Fig. 4-5, z = 0.28 cm shows the temperature distribution in the tungsten lid near the top of

UO_2 sample, $z = 0.31$ shows the temperature distribution at top of UO_2. The temperature rise near $R = 0.4$ cm is due to good contact of UO_2 and the tungsten lid near the periphery.

The axial temperature distribution (at $r = 0$) of the sample, when there is a gap formed, is shown in Fig. 4-6.

V. RESULTS

A. Determination of Ruthenium Diffusivities and Solubilities from Isothermal Diffusion Profiles

The data for each isothermal experiment were fitted to Eq. (12) using the MINUIT[71] program, thus enabling us to obtain the diffusion coefficient D and the solubility C_o of ruthenium in the uranium dioxide. A typical fit to the data is shown in Fig. 3-19. By varying the temperature of the experiment, D and C_o were determined at different temperatures. The results and the pertinent experimental conditions for these experiments are tabulated in Table 5-1. The initial position of interface, x_o, was also determined by data fitting since it was not accurately measurable. The calculated initial interface location usually coincided with the experimentally measured value to within 50 μm.

In some of the earlier annealing experiments, the alignment tube (Fig. 3-6) was made of molybdenum. In most of later experiments, tungsten alignment tubes and tungsten separators were used. The O/U ratios of the UO_2 samples annealed in two different tubes were slightly different. The O/U ratio of two of the samples were determined gravimetrically by oxidizing the reduced specimen to $UO_{2.00}$ by flowing H_2O/H_2 gas with appropriate oxygen potential over the sample at high temperature and measuring the weight gain. The O/U ratio of 7-14-1 sample, using molybdenum alignment tube, was determined to be 1.996. The O/U ratio of 9-12-2 sample, using tungsten as the alignment tube, was determined to be 1.998.

Table 5-1. Experimental conditions and results of isothermal diffusion of ruthenium in UO_2 (in flowing 4% H_2 and 96% Ar).

Sample number	Thermal history	Ruthenium form	Alignment tube and separator	Diffusivity (cm^2/sec)	Solubility ($\frac{g\ atoms\ Ru}{g\ atoms\ U}$)	Interface position x_o (μm)	χ^2 [a]
7-14-1	2150°C for 3 hrs 2130°C for 10.5 hrs	powder	molybdenum	6.7×10^{-9}	2.1×10^{-3}	- 38	2.1
7-14-2	2150°C for 3 hrs 2130°C for 10.5 hrs	powder	molybdenum	1.4×10^{-8}	4.6×10^{-3}	22	0.6
7-18-1	2060°C for 8 hrs 2040°C for 3.5 hrs	powder	tungsten	2.2×10^{-10}	2.5×10^{-3}	25	5.7
7-18-2	2060°C for 8 hrs 2040°C for 3.5 hrs	powder	tungsten	1.7×10^{-10}	1.9×10^{-3}	32	4.3
8-15	2160° for 36 hrs	disc	tungsten	1.0×10^{-9}	2.6×10^{-3}	9	0.8
9-12-1[c]	2270°C for 31 hrs	powder	tungsten	2.6×10^{-9}	3.7×10^{-2}	- 40	0.4
9-12-2[d]	2270°C for 31 hrs	powder	tungsten	2.1×10^{-9}	2.3×10^{-2}	- 14	1.1
11-4-2	2200°C for 24 hrs	powder	tungsten	5.0×10^{-10}	7.1×10^{-3}	50	2.0
11-7-1	2230°C for 24 hrs	powder	tungsten[b]	1.3×10^{-8}	1.5×10^{-2}	- 41	1.3
11-7-3	2230°C for 24 hrs	powder	tungsten	1.0×10^{-9}	9.0×10^{-3}	15	1.9
11-12-1	2300°C for 24 hrs	powder	tungsten[b]	2.5×10^{-8}	1.4×10^{-2}	3.1	1.1
11-12-2	2300°C for 24 hrs	powder	tungsten	4.0×10^{-9}	3.8×10^{-2}	- 35	0.6
11-12-3	2300°C for 24 hrs	powder	tungsten	2.0×10^{-9}	3.3×10^{-2}	- 14	1.7

[a] χ^2 based on sum of squares of errors in function normalized by standard fractional error in function data. The numbers given are standard errors per data point. Function standard error = 10.0 per cent.

[b] UO_2 in contact with molybdenum yoke.

[c] Photomicrograph shown in Fig. 3-17.

[d] Distribution shown in Fig. 3-19.

B. Diffusion Coefficient of Ruthenium in Uranium Dioxide

The Arrehenius plot of log diffusivity vs. reciprocal temperature is shown in Fig. 5-1. The data are quite scattered, which may be due to the difference in grain size of the samples, as pointed out by Butler and Meyer[54] and Reiman and Lundy.[53] All data from annealing in tungsten alignment tube and separator, except 11-7-1 and 11-12-1, fall on a straight line described by $D = D_0 e^{-E/RT}$, where D_0 is a pre-exponential factor and E is the activation energy of diffusion. One possible explanation for the high diffusivity values in specimens 11-7-1 and 11-12-1 is that these samples were in contact with the bottom of the molybdenum yoke as shown in Fig. 3-6. These two samples behaved like samples sintered in the apparatus with molybdenum fittings (7-14-1, 7-14-2).

Fitting of the data using MINUIT for samples contained in tungsten tubes (except data points 11-7-1 and 11-12-1) is shown as line (b) in Fig. 5-1. This line is characterized by E = 127.7 kcal/mole and $D_0 = 1.55 \times 10^2$ cm^2/sec. For the data of samples contained in molybdenum tubes and separators and samples 11-7-1 and 11-12-1, fitting produces E = 83.4 kcal/mole and $D_0 = 2.8 \times 10^{-1}$ cm^2/sec [line (a)]. The statistical errors in fitting the diffusivity data to obtain values of D_0 and E are given in Table 5-2. Although there are not enough data from experiments conducted in molybdenum tubes for definite proof, it is conceivable that the effective diffusivity of ruthenium in UO_2 may be affected by the crucible material.

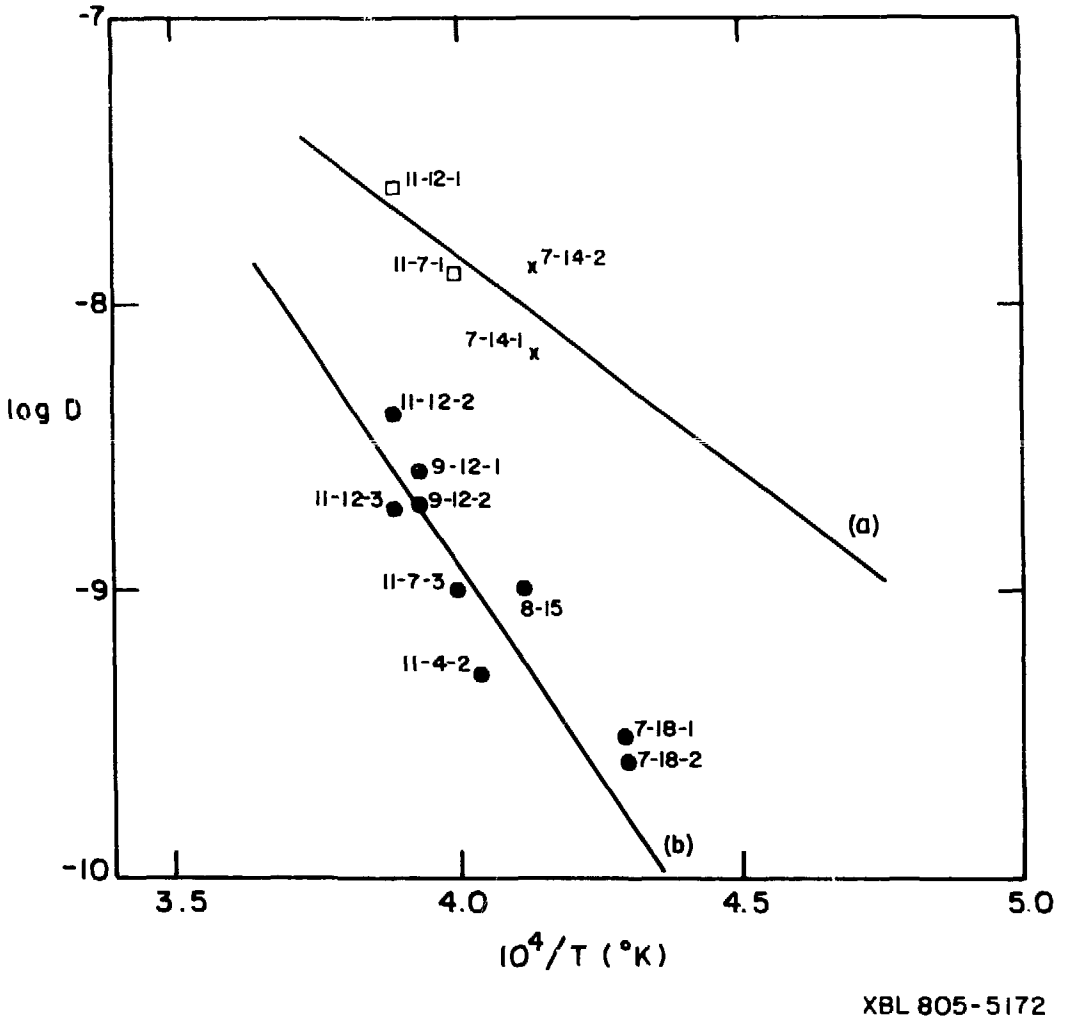

Fig. 5-1. Diffusivity of ruthenium in UO_2 vs. temperature.
x = molybdenum alignment tube and separator;
• = tungsten alignment tube and separator;
□ = tungsten alignment tube and separator, sample in contact with molybdenum yoke.

TABLE 5-2. Values and errors computed by MINUIT in fitting experimental data.

Property	Pre-exponential Factor		Activation Energy		Minimum Chi[a]
	Value pre-exponential factor	Error[b]	Value E (kcal/mole)	Error	
Diffusivity of ruthenium in UO_2 when sample is contained in tungsten crucible (line b in Fig. 5-1)	1.55×10^{2}	1.41×10^{1}	127.7	0.5	0.34
Diffusivity of ruthenium in UO_2 when sample is contained in molybdenum crucible (line a in Fig. 5-1)	2.81×10^{1}	2.51×10^{-2}	83.4	0.4	0.24
Solubility of ruthenium in UO_2	6.46×10^{10}	6.22×10^{9}	147.2	0.5	0.44

[a] Chi = average error per data point, is an indication of the overall fit.

[b] Perturbing "value" of parameter by "error" resulted in increase in average error per data point (chi) of 10%.

C. Solubility of Ruthenium in Uranium Dioxide

The Arrehenius plot of log solubility C_o of ruthenium in urania vs. reciprocal temperature is shown in Fig. 5-2. The values exhibit good straight line behavior, represented by

$$C_o = C_o' \, e^{-E_o/RT}$$

where E_o is the heat of solution of ruthenium in urania,

C_o' is the pre-exponential factor.

By fitting all of the data points, we get E_o = 147.2 kcal/mole and $C_o' = 6.5 \times 10^{10}$ g atoms Ru/g atoms U. The statistical error in fitting the data to obtain the value of C_o' and E_o are given in Table 5-2. The best-fit curve is shown as the solid line in Fig. 5-2. The solubility of ruthenium in urania does not appear to depend on the material in direct contact with the specimen.

D. The Soret Effect in Temperature Gradient Annealing Experiment

The results from the temperature gradient annealing experiment are shown in Fig. 3-21. The asymmetric profile can be caused by both the variation of diffusivity with temperature and the Soret effect. In order to determine the influence of the latter on the diffusion profile, we have to solve Eq. (13) numerically. For convenience, we rewrite Eq. (13) as

$$\frac{\partial \theta}{\partial \tau} = \frac{\partial}{\partial z}\left\{\exp\left(-E\left[\frac{T_o}{T} - 1\right]\right)\left(\frac{\partial \theta}{\partial z} + \theta M\right)\right\} \qquad (13a)$$

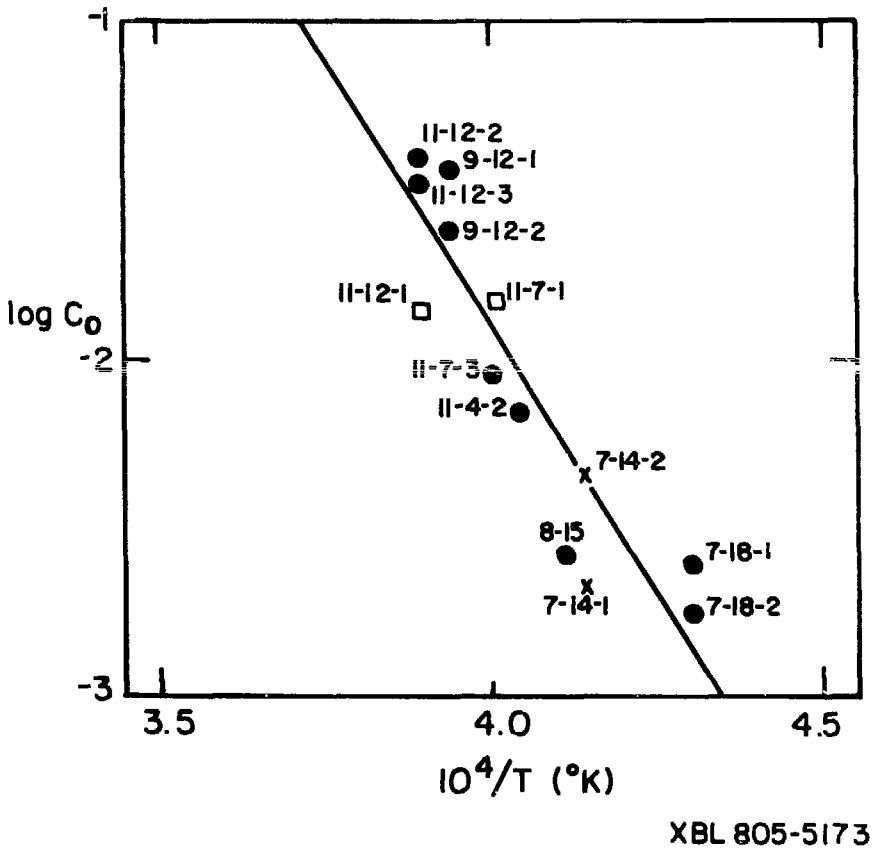

Fig. 5-2. Solubility of ruthenium in UO_2 vs. temperature.
x = molybdenum alignment tube and separator;
• = tungsten alignment tube and separator;
□ = tungsten alignment tube and separator, sample in contact with molybdenum yoke.

with I.C. $\theta(z, 0) = 0$ for $z > 0$

B.C. $\theta(0, \tau) = 1$

$\theta(\infty, \tau) = 0$

where $\theta = \frac{C}{C_o}$

$\tau = D_o t$

$E = \frac{E_d}{kT_o}$

$M = \frac{Q^* \nabla T}{k T_o^2}$

T is temperature; T_o is the temperature at the wafer-pellet interface ($z = 0$) where the ruthenium layer was deposited; C_o is the effective solubility of ruthenium in UO_2 at temperature T_o; E_d is the activation energy of ruthenium diffusion in UO_2; Q^* is the heat of transport for this diffusion process; z is distance away from the original ruthenium layer; t is time.

The solutions to Eq. (13a), using the axial temperature distribution at $r = 0$ (as shown in Fig. 4-4) and the results from isothermal annealing experiments, are shown in Fig. 5-3. For $E = M = 0$, the solution to Eq. (13a) is $\theta = \text{erfc}\left(\frac{z}{2\sqrt{\tau}}\right)$, this describes the diffusion profile in an isothermal annealing experiment from an inexhaustible plane source at $z = 0$. For $T_o = 2260°C$ and $\tau = 5.02\ 10^{-4}$ cm^2 ($t = 40$ hrs) the diffusion profile, which is symmetrical with respect to the original ruthenium layer ($z = 0$), is shown as curve a in Fig. 5-3. Curve b, with $E = 25$ ($E_d = 127$ kcal/mole, $T_o = 2260°C$), $M = 0$ ($Q^* = 0$), shows the

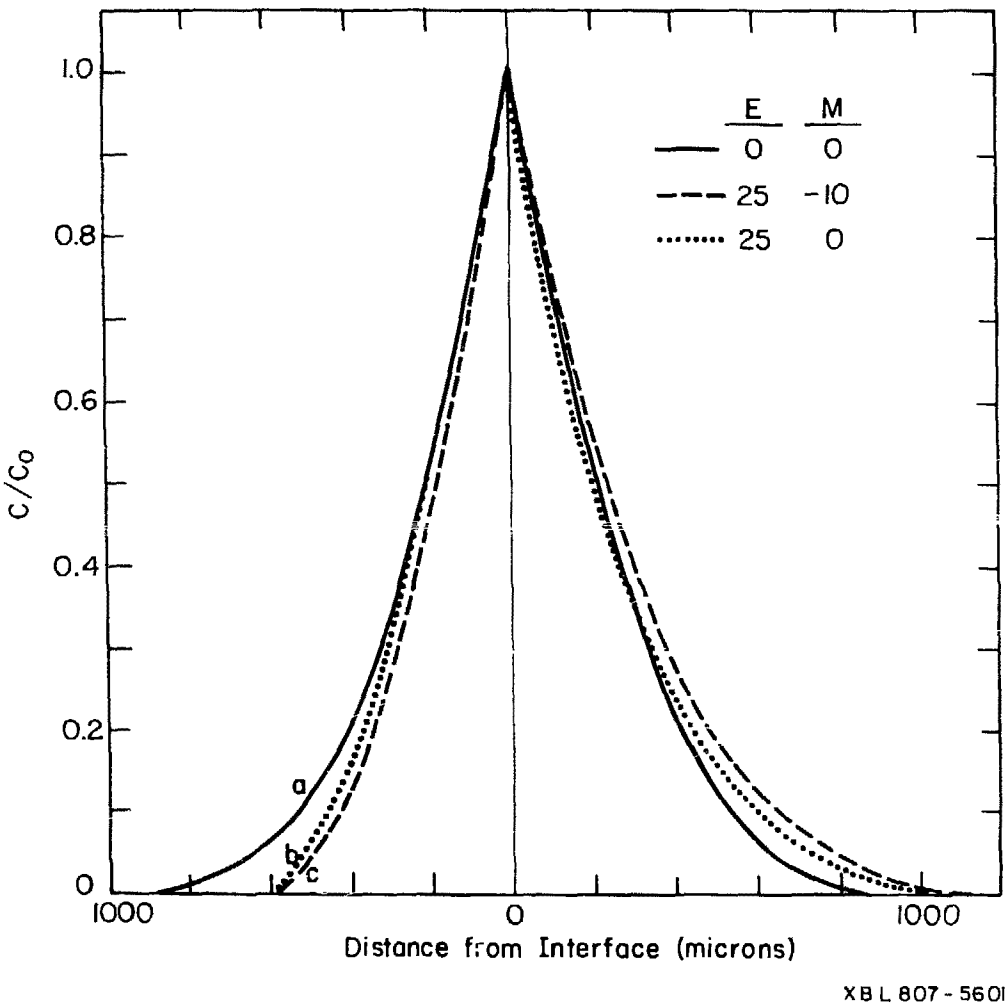

Fig. 5-3. Calculated diffusion profile of ruthenium in UO_2.

effect of temperature gradient on the diffusion profile, when there is no Soret effect. Notice this curve is not symmetrical with respect to $z = 0$. For $E = 25$ and $M = -10$ ($Q^* = 100$ kcal/mole), curve c shows the influence of Soret effect on the diffusion profile. There is not much difference between curves b and c. In other words, according to simple diffusion theory, the influence of Soret effect on the diffusion profile is small.

We tried to use axial surface average temperature

$$\bar{T} = \frac{\int_0^R 2\pi r\, T(r)\, dr}{\pi R^2} ,$$

instead of the central temperature, in the numerical calculation to see the effects of temperature and temperature gradient on the diffusion profile. The temperature gradient is about the same (~1350°C/cm) in the two calculations. The results are similar to those shown in Fig. 5-3, except that the spread is smaller for the same amount of time (due to lower temperatures).

The calculated results (Fig. 5-3) and the experimental results (Fig. 3-21) are very different. The calculated concentration drops from the interface very fast, like an error function, while the experimental results (Fig. 3-21) have a round shoulder and do not drop very fast at the hot side of the interface. The ruthenium concentrations in the wafer near the interface are higher than the solubility at the interface. The position of the interface is known fairly accurately by visual inspection during the grinding process and the dimension of the UO_2 wafer before the annealing experiment. The maximum experimental error concerning

the position of the interface is estimated to be less than 100 microns. However, the temperature distribution in the sample is not known very well. The solubility is very sensitive to the temperature; the solubility reported in Fig. 5-3 is the solubility for the calculated temperature. Therefore, it is uncertain what the true solubility is at the interface. At the moment, we cannot explain the results of the temperature gradient annealing experiment with our simple diffusion model.

Another factor that would affect the concentration distribution of ruthenium is the oxygen potential gradient created by the temperature gradient. This gradient in the activity of oxygen would make ruthenium migrate in addition to the soret effect mentioned earlier.

VI. DISCUSSION

A. Thermal Migration of Metallic Inclusions in Urania

Post irradiation analysis of reactor fuels has revealed metallic inclusions in the irradiated fuel.[1-11] A few investigators[12,13,17] believe that under the influence of temperature gradient, the movement of uranium dioxide atoms along the inclusion-matrix interface causes the inclusion to move bodily up the temperature gradient. However, from our experiments (described in Section C-3 of Chapter 3) the solid inclusions (tungsten and molybdenum) do not move bodily when subjected to a temperature gradient of 1000°C/cm at 2500°C for 12-36 hrs. Isothermal annealing of ruthenium layers in UO_2 suggested that ruthenium diffuses atomically along grain boundaries in unsaturated uranium dioxide. Bodily migration and atomic diffusion of the fission products probably occur simultaneously in the fuel. The importance of each mechanism depends on the chemical and thermal conditions in the fuel. We speculate that the metallic inclusions observed in irradiated fuel were formed in the following manner: During operation of the reactor, the concentration of each fission product depends on the neutron flux, the concentration of the fissile material, and the duration of irradiation. Before the solubility limit of each fission product in the fuel is reached, each fission product diffuses atomically in the fuel under the influence of concentration gradient and thermal gradient (Soret effect). In addition, the fission product reacts with the fuel and other fission products.

The extent of reaction depends strongly on the local temperature and the oxygen potential. Once the solubility limit of one particular fission product in the oxide fuel is exceeded, that fission product precipitates out as inclusions. If these precipitates are solid, they are either immobile or their bodily migration rate is very slow, as shown in Section C-3 of Chapter 3. If the inclusions are liquid, the thermal migration rate may be much faster. There have been many studies demonstrating the thermal migration of liquid inclusions.[31-34] Some studies suggest that the metallic inclusions found in the fuel might be liquid during the operation of the reactor. These liquid metallic inclusions migrate, up the concentration gradient of each constituent in the inclusion, (i.e., up the temperature gradient.) This explains why most inclusions were found in the columnar grain regions and the central void, not in the colder region of the fuel (they remain as atoms here). Another fact learned from our study (Section C-1 of Chapter 3) is that some inclusions examined in post-irradiation analysis do not necessarily exist at high temperatures. They can be dissolved in the matrix at high temperature and precipitate out during cooling down.

In Poeppel's experiment,[12] trails were observed behind the moving inclusions. These trails could have been formed by the bodily motion of liquid inclusions.[65] This may explain why we did not observe the migration of inclusions or trails when using molybdenum and tungsten as inclusions.

Schumacher et al.[13] observed that inclusions became bigger after thermal gradient heat treatment and the volume percent of inclusions are constant with radius. However, there was really no direct

evidence and data to support their speculation that this coalescence was caused by bodily migration and coagulation of smaller inclusions. We think that in their samples atomic diffusion and bodily migration occurred simultaneously.

B. Diffusion Mechanism of Ruthenium in Urania

From the ruthenium disk experiment (Section C-4 of Chapter 3), we know that the transport of ruthenium in UO_2 proceeds by atomic dissolution and atomic diffusion processes. Figure 3-17 and the single crystal experiment showed that the diffusion path was the grain boundaries. There is no detectable ruthenium penetration in the lattice. The pre-exponential factor and the activation energy for lattice and grain boundary diffusion in ceramic material measured by other workers[52-57,64] are tabulated in Table 6-1 for comparison.

Microprobe analysis shows that the metallic inclusions at grain boundaries consist of metallic uranium and ruthenium. There are two possibilities on how the U-Ru intermetallic compound is formed at grain boundaries. One possibility is that the intermetallic compound is formed at high temperature during the annealing experiment, the other is that it is formed while the sample was cooling down. The second possibility seems unlikely however. We assume that the intermetallic compound is formed at high temperature.

From Lewis acid-base theory,[59] ruthenium and uranium should form very stable intermetallic compounds. The phase diagram shows that U Ru_2, URu, U_3Ru_4, U_2Ru_3, U_3Ru_5, and URu_3 are all possible U-Ru compounds.[46,47]

Table 6-1. Values of grain boundary diffusivities $D_{gb} = D_{gb}^{o} e^{-E_{gb}/kT}$ and lattice diffusivity $D_{\ell} = D_{\ell}^{o} e^{-E_{\ell}/kT}$.

Material	D_{gb} (cm^2/sec)		D_{ℓ} (cm^2/sec)		Reference
	D_{gb}^{o} (cm^2/sec)	E_{gb} (kcal/mole)	D_{ℓ}^{o} (cm^2/sec)	E_{ℓ} kcal/mole)	
Uranium self-diffusion UO_2	8.7×10^{-2}	4.7	5.8×10^{-5}	72.7	(64)
Plutonium self-diffusion in $(U.Pu)O_{1982}$ at T = 2223°K	3×10^{-10}		8.4×10^{-15}		(52)
Protactinium in ThO_2	1.1×10^{-3}	30.6	2.91×10^{-5}	75	(55)
Protactinium in ThO_2-UO_2	1.0	59.7	1.88	91.8	(55)

Since our sample is only slightly substoichiometric, the activity of uranium metal is not very high, the most stable compound would be URu_3. Work by Holleck and Kleykamp[60,61] and Paszkowicz[62] proved the existence of URu_3 and indicated the high stability of this intermetallic compound. Another interesting aspect, demonstrating the existence of this stable intermetallic phase, is the occurrence of the metallic phase $(U,Pu(Ru, Rh, Pd)_3)$ in oxide fuel at high burnups.[7,63]

The diffusion mechanism in a reducing atmosphere involves ruthenium atoms migrating along the grain boundaries. The ruthenium then reacts with the substoichiometric uranium oxide and forms the intermetallic compound URu_3 by the following reaction

$$UO_{2-x}(s) + 3Ru(s) \rightleftharpoons URu_3(\ell) + \frac{2-x}{2} O_2(g) \quad . \qquad (36)$$

The URu_3 precipitates out as a second phase in the grain boundaries as it is formed. The constant removal of ruthenium as the precipitates URu_3, increases the concentration gradient of ruthenium atoms and hence increases the flux of ruthenium into uranium oxide. Therefore, our data interpretation, which is based on simple diffusion theory, produced an "effective" diffusion coefficient of ruthenium in uranium dioxide.

C. Stability of URu_3 in UO_{2-x}

At a given temperature, there is a unique oxygen pressure $P^*_{O_2}$ at which both Ru and URu_3 can coexist in UO_{2-x}. In addition, RT ℓn $P^*_{O_2}$ must be equal to the oxygen potential of UO_{2-x} at temperature T.

Eq. (36) can be broken down into 3 subreactions:

$$\text{(i)} \quad UO_{2-x}(s) + \frac{x}{2} O_2(g) = UO_2(s) \tag{37}$$

$$\Delta G^o = -\frac{1}{2}\int_o^x \Delta \bar{G}_{O_2} dx'$$

where $\Delta \bar{G}_{O_2}$ is the oxygen potential of UO_{2-x} at temperature T.

$$\text{(ii)} \quad U(\ell) + O_2(g) = UO_2(s) \tag{38}$$

The standard free energy of formation of UO_2 is $\Delta G^o_{fUO_2}$.

$$\text{(iii)} \quad U(\ell) + 3\,Ru(s) \rightleftharpoons URu_3(\ell) \tag{39}$$

The standard free energy of formation is $\Delta G^o_{fURu_3}$.[60]

(i) and (ii) yield

$$U(\ell) + \frac{2-x}{2} O_2(g) = UO_{2-x}(s) \tag{40}$$

and

$$\Delta G^o_{fUO_{2-x}} = \Delta G^o_{fUO_2} + \frac{1}{2}\int_o^x \Delta \bar{G}_{O_2}\, dx'. \tag{41}$$

Subtracting (40) from (39), we have the overall reaction, Eq. (36) and the standard free energy of formation of Eq. (36) is ΔG^o_R

$$\Delta G^o_R = \Delta G^o_{fURu_3} - \Delta G^o_{fUO_{2-x}}. \tag{42}$$

The oxygen pressure at which Eq. (36) is in equilibrium with is

$$\left(P^*_{O_2}\right)^{\frac{2-x}{2}} = e^{-\Delta G^o_R/RT} \quad . \tag{43}$$

But the oxygen potential of UO_{2-x}, $\Delta\bar{G}_{O_2}$, can be expressed as

$$\Delta\bar{G}_{O_2} = RT \ln P^*_{O_2} \quad . \tag{44}$$

Combining Eqs. (41), (42), (43), and (44), we have

$$\Delta G^o_R + \frac{2-x}{2}\,\Delta\bar{G}_{O_2} = 0 \tag{45}$$

or

$$\Delta G^o_{fURu_3} = \Delta G^o_{fUO_2} + \frac{1}{2}\int_o^x \Delta\bar{G}_{O_2}\,dx' - \frac{2-x}{2}\,\Delta\bar{G}_{O_2} \quad . \tag{46}$$

The value of $\Delta G^o_{fUO_2}$ can be expressed as[66]

$$\Delta G^o_{fUO_2} = -1080 + 167\ (T(°K)/1000)\ \ KJ/mole \quad . \tag{47}$$

Since the value of $\bar{G}_{O_2}$ is a known function of x and temperature T,[67-70] Eq. (46) can be solved for the critical stoichiometry $(O/U)^*$ (for each T) at which Ru and URu_3 coexist in UO_{2-x}. For $O/U < (O/U)^*$, URu_3 is the stable form; for $O/U > (O/U)^*$, metallic ruthenium is stable. Equation (46) is plotted in Fig. 6-1, using $\Delta\bar{G}_{O_2}$ values given by Blackburn.[69] The intersection of the two curves gives the critical value $(O/U)^*$, which is 1.990 at 2450°K. The experimental value (1.996) is higher than the value predicted by using Blackburn's model to calculate the $\Delta\bar{G}_{O_2}$. However, our sample was polished using water as a lubricant,

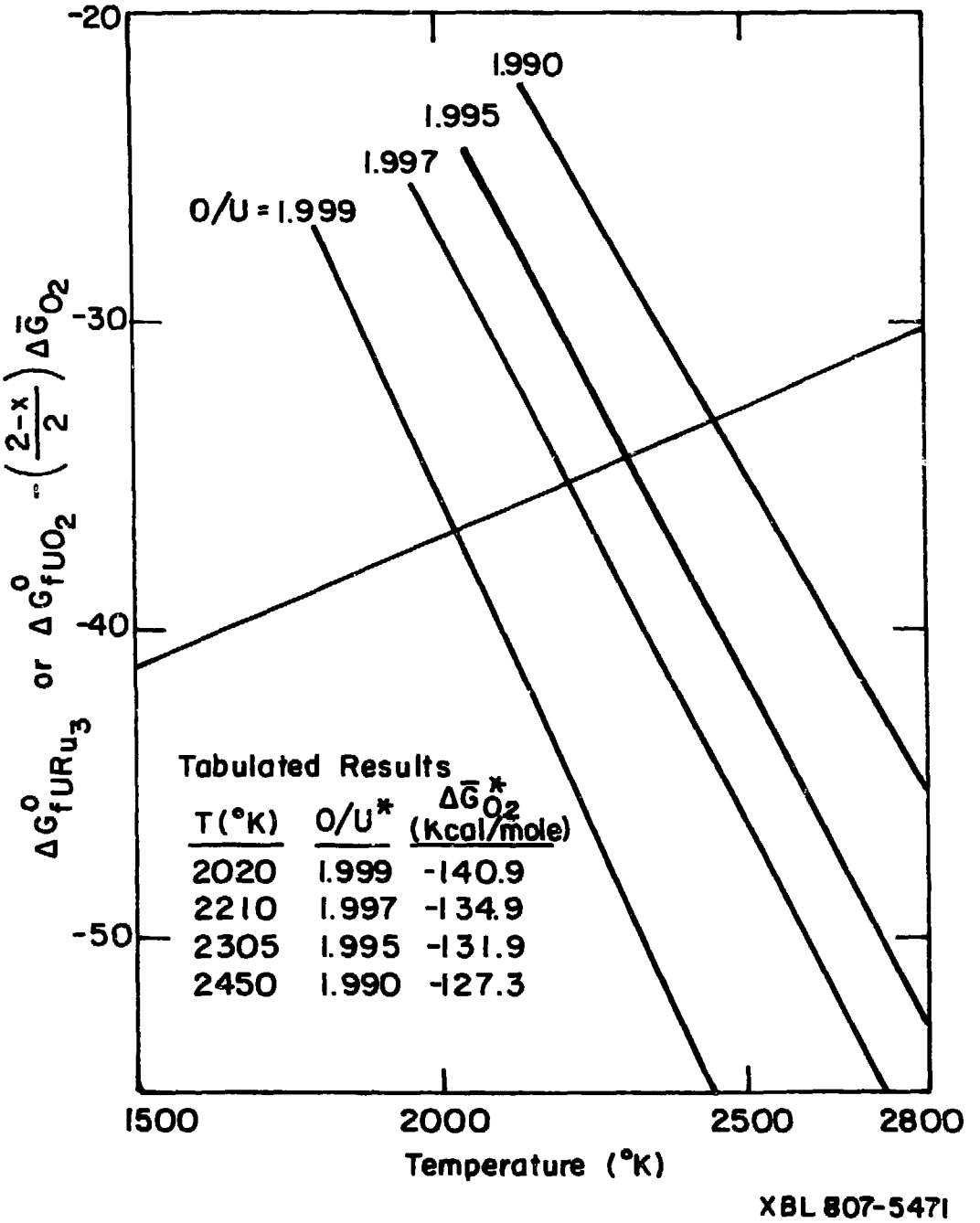

Fig. 6-1. $(O/U)^{*}$ as a function of temperature for URu_3 in UO_{2-x}.

exposed in air for a long period of time before the stoichiometry was examined. The value we reported could be higher than the stoichiometry of the sample during the anneal experiment.

Alternatively, the critical H_2O/H_2 ratio at the gas phase can be calculated from the equilibrium constant of the reaction:

$$H_2(g) + \frac{1}{2} O_2(g) = H_2O\ (g) \tag{48}$$

The standard free energy of formation is $\Delta G^o_{fH_2O}$ and

$$RT\ \ell n\left(\frac{P_{H_2O}}{P_{H_2}}\right)^* = -\Delta G^o_{f\,H_2O} + \frac{1}{2}\Delta \bar{G}_{O_2}(O/U^*, T) \tag{49}$$

$$\left(\frac{P_{H_2O}}{P_{H_2}}\right)^* \quad \text{for } (O/U)^* = 1.99, \quad T = 2450°K.$$

is $$\left(\frac{P_{H_2O}}{P_{H_2}}\right)^* \cong 10^{-4}.$$

In our system, we have used a purified dry hydrogen - argon gas mixture, so the H_2O/H_2 ratio must have been smaller than 10^{-4}. Therefore, URu_3 formation is favored.

D. Diffusivity of Ruthenium in Uranium Dioxide Annealed in Molybdenum and Tungsten Crucibles

As shown in Fig. 5-1, the diffusivities of ruthenium in uranium dioxide were found to be strongly dependent upon the metal used to contain the specimen during the anneal. The diffusivities were larger when the alignment tube and separator were of molybdenum than when tungsten was used.

One reasonable explanation for the observed difference in diffusivities is that these properties of the ruthenium-uranium oxide interaction are strongly dependent on the stoichiometry of urania. At high temperatures, molybdenum is more permeable to oxygen and is more easily oxidized than is tungsten. In the former, the urania is more easily reduced by the flowing hydrogen-argon mixture gas in which the anneal is conducted, since the activity of uranium is higher in the urania contained in the molybdenum crucible than in that of the tungsten crucible. Reaction (39) is enhanced in the former samples and more URu_3 is formed. This constant removal of ruthenium from grain boundaries to form URu_3 would enhance the concentration gradient of ruthenium and hence increase the flux. Therefore, higher diffusivities are observed in samples annealed in molybdenum crucible. However, in our case the difference in $\Delta\bar{G}_{O_2}$ (for 7-14-1, $\Delta\bar{G}_{O_2}$ = -120 kcal/mole, 9-12-2 is -108 kcal/mole, according to Blackburn's model[69]) is not very large. It is uncertain that this small difference in oxygen potential could cause such a large difference in diffusivities.

Another factor which may cause the effective diffusivity

difference is impurities in the crucible. As indicated by Holleck,[60,61] when carbon was present in the U-Ru system, a more stable compound, URu_3C_x, was formed. The molybdenum crucibles we used in annealing experiment were machined from forged molybdenum rod, which may have contained carbon. The presence of carbon in the molybdenum could enhance the formation of URu_3C_x and therefore would increase the effective diffusivity. The tungsten crucibles, however, were made by chemical vapor deposition method. There is no carbon involved in the process; therefore no carbon impurity in the tungsten crucibles.

E. Applicability of Experimental Results and Sources of Errors

Since the diffusion path in ruthenium annealing experiment involved mainly the grain boundaries, the grain size plays an important role in the measured diffusivities. The diffusivities measured in this experiment are only applicable to UO_2 with grain size similar to our sample. (See Section A of Chapter 3 for sample description). Moreover, the grain size is not uniform over the entire sample. In some areas the grains are significantly larger than other areas.

There are a number of "unavoidable" sources of errors encountered in this experiment. Their significance are discussed below:

(i). The integrity of the bond between UO_2 wafer and pellet. When the polished UO_2 contact surfaces are not smooth and parallel to each other over the entire contact surface, there could be a partial gap at interface. This incomplete bonding at the interface would interfere the diffusion process and

resulted in non-uniform diffusion front. Fractures and cracks which occur during annealing would affect the diffusion result significantly.

(ii). The original deposit of ruthenium powders at the pellet-wafer interface is not uniform. This non-uniformity in the initial ruthenium concentration would result in non-uniform diffusion front. The analysis of x-ray fluorescence spectrometry was based on the assumption that the ruthenium is uniformly distributed in uranium dioxide. The error is enhanced in our situation by the fact that the intensity of the x-ray beam is not uniform across the whole sample. It is difficult to estimate how big an error is introduced due to the non-uniformity of the initial ruthenium distribution and the incident x-ray beam. We tried to minimize these errors by depositing several layers of ruthenium powders and by putting the sample in the x-ray fluorescence machine with the same orientation each time.

(iii). Some errors would be introduced if the exposed surfaces are not parallel to the original ruthenium plane. We used a special fixture made by Buehler Co. to grind our samples. After each grinding, the samples were checked for parallelism. The samples were found to be parallel to the original ruthenium plane to within 50 μm.

(iv). In the temperature gradient annealing experiment, as described in Section E of Chapter 5, we treated the problem as one dimensional. It is actually a two dimensional process as shown by the fact that after the temperature gradient annealing, ruthenium - uranium alloy concentrated in the central region.

F. Recommendations for Future Experiments

(i). Since grain size plays an important role in the measurement of diffusivity, use of an isostatic pressing procedure when preparing UO_2 samples is strongly recommended. With this

technique more uniform grain sizes can be obtained over the entire sample.

(ii). Using samples with different initial grain size to study the effect on the measured diffusion coefficients.

(iii). By annealing ruthenium in single crystal uranium dioxide over a long period of time, (e.g., 100 hrs) the lattice diffusivity and solubility of ruthenium in uranium oxide could be determined.

(iv). Study the effect of oxygen potential on the diffusivity of ruthenium in uranium oxide.

(v). In the thermal gradient annealing experiment, transport of oxygen toward the cold side occurs. Care should be taken in measuring the heat of transport of ruthenium in the oxide under such conditions. The effect of oxygen redistribution should be accounted for.

(vi). As discussed in Section C of this Chapter, the impurity in the crucible, especially carbon, may play an important role in the rate of diffusion. Each crucible should be cleaned by heating in vacuum at high temperature before use in diffusion experiments.

REFERENCES

1. J. I. Bramman and H. J. Powell, "Redistribution of Fuel and Fission Products in Irradiated Oxide Fuel Pins," J. Br. Nucl. Energy Soc. 14, No. 1 (1975) 63.

2. B. T. Bradbury, J. T. Demant, P. M. Martin and D. M. Poole, "Electron Probe Micro-analysis of Irradiated UO_2," J. Nucl. Mater. 17 (1965) 227.

3. B. T. Bradbury, J. T. Demant, and P. M. Martin, "Solid Fission Products in Irradiated Uranium Dioxide," UKAEA Report AERE-R5149 (1966).

4. B. M. Jeffery, "Micro-analysis of Inclusions in Irradiated UO_2," J. Nucl. Mater. 22 (1967) 33.

5. J. L. Bates, "Metallic U in Irradiated UO_2," Hanford USAEC Report HW-82263 (1964).

6. D. R. O'Boyle, F. L. Brown and J. E. Sanecki, "Solid Fission Product Behavior in $(U.Pu)O_2$ Fuel Irradiated in a Fast Neutron Flux," J. Nucl. Mater. 29 (1969) 27.

7. J. I. Bramman, R. M. Sharpe, D. Thom and G. Yates, "Metallic Fission Product Inclusions in Irradiated Oxide Fuel," J. Nucl. Mater. 25 (1968) 201.

8. J. H. Davies, R. F. Boyle, B. Weidenbaum and J. E. Hanson, "On the Composition of Metallic Ingots Formed in High-Performance Ceramic Fuel Element," ANS Trans. 9 (1) (1966) 63.

9. H. Kleykamp, "The Chemical State of Irradiated Uranium-Plutonium Oxide Fuel Pins," International Conference on Fast Breeder Reactor Fuel Performance, Proc. Symp. (Monterey, Ca. 1979) 393.

10. D. R. O'Boyle, F. L. Brown and A. E. Dwight, "Analysis of Fission Product Ingots Formed in Uranium-Plutonium Oxide Irradiated in EBR-II," J. Nucl. Mater. 35 (1970) 257.

11. M. Conte, M. Mouchnino and F. K. Schmitz, "Postirradiation Observations of Mixed Oxides with Initial Addition of Fission Product Elements," Nucl. Tech. 16 (1972) 143.

12. L. C. Michels and R. B. Poeppel, "In Pile Migration of Fission Product Inclusions in Mixed Oxide Fuel," J. Appl. Phys. 44, No. 3 (1973) 1003.

13. F. D'Annucci, C. Sari and G. Schumacher, "Migration of Metallic Fission Product in Reactor Oxide Fuels," Nucl. Tech. 35 (1977) 80.

14. G. Giacchetti and C. Sari, "Behavior of Molybdenum in Mixed-Oxide Fuel," Nucl. Tech. 31 (1976) 62.

15. F. L. Brown, L. A. Niemark and J. E. Ayer, "Performance of Vibratorily Compacted Mixed-Oxide Fuel Elements in EBR-II to 2.7 at % Burnup," ANL-7954 (1970).

16. J. Bates, J. A. Christensen and W. E. Roake, "Fission Products and Plutonium Migration in Uranium-Dioxide Fuel," Nucleonics 20, No. 3 (1962) 88.

17. F. A. Nichols, "Transport Phenomena in Nuclear Fuels Under Severe Temperature Gradient, J. Nucl. Mater. 84 (1979) 1.

18. S. R. deGroot, "Thermodynamics of Irreversible Process," North-Holland Publishing Co., Amsterdam (1951).

19. S. R. deGroot, and P. Mazur, "Non-Equilibrium Thermodynamics," North-Holland Publishing Co., Amsterdam (1962).

20. K. G. Denbigh, "The Thermodynamics of Steady State," Methuen & Co., LTD., London (1951).

21. M. Bober and G. Schumacher, "Material Transport in the Temperature Gradient of Fast Reactor Fuels," Advances in Nuclear Science Technology, Vol. 7 (1973) 121.

22. A. R. Allnatt and A. V. Chadwick, "Thermal Diffusion in Crystalline Solids," Chem. Rev. 67 (1967) 681.

23. Ya. E. Geguzin and M. A. Krivoglaz, "Migration of Macroscopic Inclusions in Solids," Plenum Press (1973).

24. F. A. Nichols, "Kinetics of Diffusional Motion of Pores in Solids," J. Nucl. Mater. 30 (1969) 143.

25. H. S. Carslaw and J. C. Jaeger, "Conduction of Heat in Solids," Second ed. Oxford Press (1959) 426.

26. C. F. Clement and M. W. Finnis, "The Movement of Lenticular Pores in Mixed Oxide Nuclear Fuel Element," J. Nucl. Mater. 75 (1978) 115.

27. F. A. Nichols, "On the Thermal Gradient Migration of Lenticular Voids," J. Nucl. Mater. 84 (1979) 319.

28. P. F. Sens, "The Kinetics of Pore Movement in UO_2 Fuel Rods," J. Nucl. Mater. 43 (1972) 293.

29. F. A. Nichols, "Pore Migration in Ceramic Fuel Element," J. Nucl. Mater. 27 (1968) 137.

30. H. Kawamata, H. Kaneko, H. Furuya and M. Koizuimi, "Migration Rate of Lenticular Voids in UO_2 Under the Influence of Temperature Gradient," J. Nucl. Mater. 68 (1977) 48.

31. T. R. Anthony and H. E. Cline, "Thermal Migration of Liquid Droplet Through Solids," J. Appl. Phys. 42, No. 9 (1971) 3380.

32. W. A. Tiller, "Migration of a Liquid Zone Through a Solid," J. Appl. Phys. 34, No. 9 (1963) 2757.

33. J. H. Wernick, "Determination of Diffusivities in Liquid Metals by Means of Temperature-Gradient Zone Melting," J. Chem. Phys. 25, No. 1 (1956) 47.

34. W. G. Pfann, "Temperature Gradient Zone Melting," J. Metals Trans. AIME (1955) 961.

35. D. R. H. Jones, "The Thermal Stability of Eutectic Composites in a Temperature Gradient," Metal Sci. 8 (1974) 37.

36. P. G. Shewmon, "The Movement of Small Inclusions in Solids by a Temperature Gradient," Trans. Met. Soc. AIME 230 (1964) 1134.

37. T. D. Gulden, "Carbon Thermal Diffusion in the UC_2-C System," J. Amer. Ceram. Soc. 55 (1972) 14.

38. M. McLean, "Particle Coarsening in a Temperature Gradient," Scripta Metallurgica. 9 (1975) 439.

39. P. S. Ho, "Motion of Inclusion Induced by a Direct Current and a Temperature Gradient," J. Appl. Phys. 41, No. 1 (1970) 64.

40. J. Biersack and W. Diez, "Motion of Markers and Bubbles in Solids by Self-Diffusion in a Temperature Gradient," Phys. Stat. Sol. 27 (1968) 139.

41. D. R. H. Jones and G. J. May, "The Thermal Stability of the Al-Al_3Ni Eutectic in a Temperature Gradient," Acta Metallurgica 23 (1975) 29.

42. D. C. Houghton and D. R. H. Jones, "The Thermal Stabilities of IN SITU Composites in a Temperature Gradient - I. The Al-$CuAl_2$ Eutectic," Acta Metallurgica 26 (1978) 695.

43. D. C. Houghton and D. R. H. Jones, "The Thermal Stabilities of IN SITU Composites in a Temperature Gradient - II. The Al-Al_3Ni and Cu-Cr Eutectics," Acta Meallurgica 27 (1979) 1031.

44. M. F. Ashby and R. M. A. Centamore, "The Dragging of Small Oxide Particles by Migrating Grain Boundaries in Copper," Acta Mellurgica 16 (1968) 1081.

45. A. D. Brailsford and H. B. Aaron, "Growth of Grain-boundary Precipitates," J. Appl. Phys. 40, No. 4 (1969) 1702.

46. P. M. Hansen and K. Anderko, "Constitution of Binary Alloy," Metallurgy and Metallurgical Engineering Series. Second edition. McGraw-Hill Book Co. (1958).

47. R. P. Elliot, "Constitution of Binary Alloy," First Supplement McGraw-Hill Book Co. (1965).

48. P. S. Maiya, "Surface Diffusion, Surface Free Energy, and Grain Boundary Free Energy of Uranium Dioxide," J. Nucl. Mater. 40 (1971) 57.

49. Heating 5 ORNL/CSD/TM-15.

50. Handbook of Thermophysical Properties of Solid Materials, Vol. 1, "Elements," Pergamon Press (1961).

51. MATPRO-VERSION 9. A Handbook of Material Properties for Use in the Analysis of Light Water Reactor Fuel Rod Behavior. TREE-NUREG-1005.

52. G. R. Chilton and J. Edwards, "The Solid-State Diffusion of Plutonium in Uranium Dioxide," J. Nucl. Mater. 78 (1978) 182.

53. D. K. Reiman and T. S. Lundy, "Diffusion of ^{233}U in UO_2," J. Amer. Ceram. Soc. 52 (1969) 511.

54. E. M. Butler and R. O. Meyer, "Diffusion of Plutonium and Uranium in Irradiated Mixed Oxide," J. Nucl. Mater. 47 (1973) 229.

55. H. Furuya and S. Yajima, "Lattice and Grain-boundary Diffusions of Protactinium in ThO_2 and in a ThO_2-UO_2 Solid Solution," J. Nucl. Mater. 25 (1968) 38.

56. P. G. Shewmon, Diffusion in Solids, McGraw-Hill Book Co. (1963).

57. J. Belle, "Oxygen and Uranium Diffusion in Uranium Dioxide," J. Nucl. Mater. 30 (1969) 3.

58. F. Schmitz and R. Lindner, "Diffusion of Heavy Elements in Nuclear Fuels: Actinide in UO_2," J. Nucl. Mater. 17 (1965) 259.

59. L. Brewer and P. Wengert, "Transition Metal Alloys of Extra-ordinary Stability; An Example of Generalized Lewis-Acid-Base Interaction in Metallic System," Met. Trans. 4 (1973) 83.

60. H. Holleck and H. Kleykamp, "The Constitution and Thermodynamics of the System U-Ru-C," J. Nucl. Mater. 35 (1970) 158.

61. H. Holleck, "The Effect of Carbon on the Occurrence of Cu_3Au Type Phase in Actinide and Lanthanide-Platinum Metal System," J. Nucl. Mater. 42 (1972) 278.

62. W. Paszkowicz, CEA Report, to be published.

63. F. T. Ewart, J. M. Horspool and G. James, "The Chemical Effects of Compositional Changes in Irradiated Oxide Fuel Materials - Fission Product Segregation and Chemical Equilibria," J. Nucl. Mater. 61 (1976) 254.

64. S. Yajima, H. Furuya, and T. Hirai, "Lattice and Grain Boundary Diffusion of Uranium in UO_2," J. Nucl. Mater. 20 (1966) 162.

65. Personal Communication with Dr. Poeppel.

66. D. R. Olander, "Fundamental Aspects of Nuclear Reactor Fuel Elements," Technical Information Center, Office of Public Affairs, ERDA TID-26711-P1 (1976).

67. G. H. Winslow, "An Examination of the Total Pressure Over Hypostoichiometric Uranium Dioxide," High Temp. Sci. 7 (1975) 81.

68. M. Tetenbaum and P. D. Hunt, "High-Temperature Properties of Oxygen-deficient Urania," J. Chem. Phys. 49, No. 11 (1968) 4739.

69. P. E. Blackburn, "Oxygen Pressure Over Fast Breeder Reactor Fuel," J. Nucl. Mater. 46 (1973) 244.

70. N. Javed, "Thermodynamic Study of Hypostoichiometric Uranica," J. Nucl. Mater. 43 (1972) 219.

71. MINUIT, a system for minimizing a function of n parameters and computing the parameter errors and correlation. It was developed by CERN Computer Center, now available in UC Computer.

APPENDIX A

Under the influence of temperature gradient, the velocity of an inclusion migrating in a UO_2 matrix by the surface diffusion mechanism is described by Eq. (19),

$$U = \frac{dx}{dt} = \frac{2 D_s \Omega^{1/3} Q_s^*}{k T^2} \left(\frac{\beta_s}{R}\right) \left(\frac{dT}{dx}\right)$$

where Ω is the molecular volume of UO_2 and D_s is the interfacial diffusion coefficient of UO_2 at the inclusion-matrix interface. This property is not known, so as an approximation, we use the surface diffusion coefficient of UO_2, which is,[48]

$$D_s = 5.4 \times 10^5 \exp(-453/RT) \text{ cm}^2/\text{sec} \quad . \qquad \text{(A-1)}$$

The heat of transport, Q_s^*, is not available, but 100 kcal/mole is assumed. For a linear temperature distribution, $T = T_o + (dT/dx)x$, where T_o is the temperature at $x = 0$, the initial position of the inclusion. The temperature correction factor at the inclusion-UO_2 interface is:

$$\beta_s = \frac{3k_{UO_2}}{2k_{UO_2} + \{k_i/[1 + k_i(HR)^{-1}]\}} \qquad \text{(A-2)}$$

where R is the inclusion radius, k_i is the thermal conductivity of the inclusion, and H is an interfacial heat-transfer coefficient, for which a value of 10^3 watt/cm^2/°C is suggested by Poeppel.[12] For a tungsten inclusion of 5 μm diameter, $\beta_s = 0.35$.

The velocity of a 5 μm tungsten inclusion, in a temperature gradient of 1300°C/cm, at a distance x from the initial position, is

$$\frac{dx}{dt} = \frac{3.4 \times 10^9}{(T_o + 1300\ x)^2} \exp - \frac{5.4 \times 10^4}{T_o + 1300\ x} \quad cm^2/sec \qquad (A\text{-}3)$$

Using the Runge-Kutta method to integrate Eq. (A-3) numerically, we calculate the position of the inclusion at various times for several initial temperatures. The results are shown in Fig. A-1.

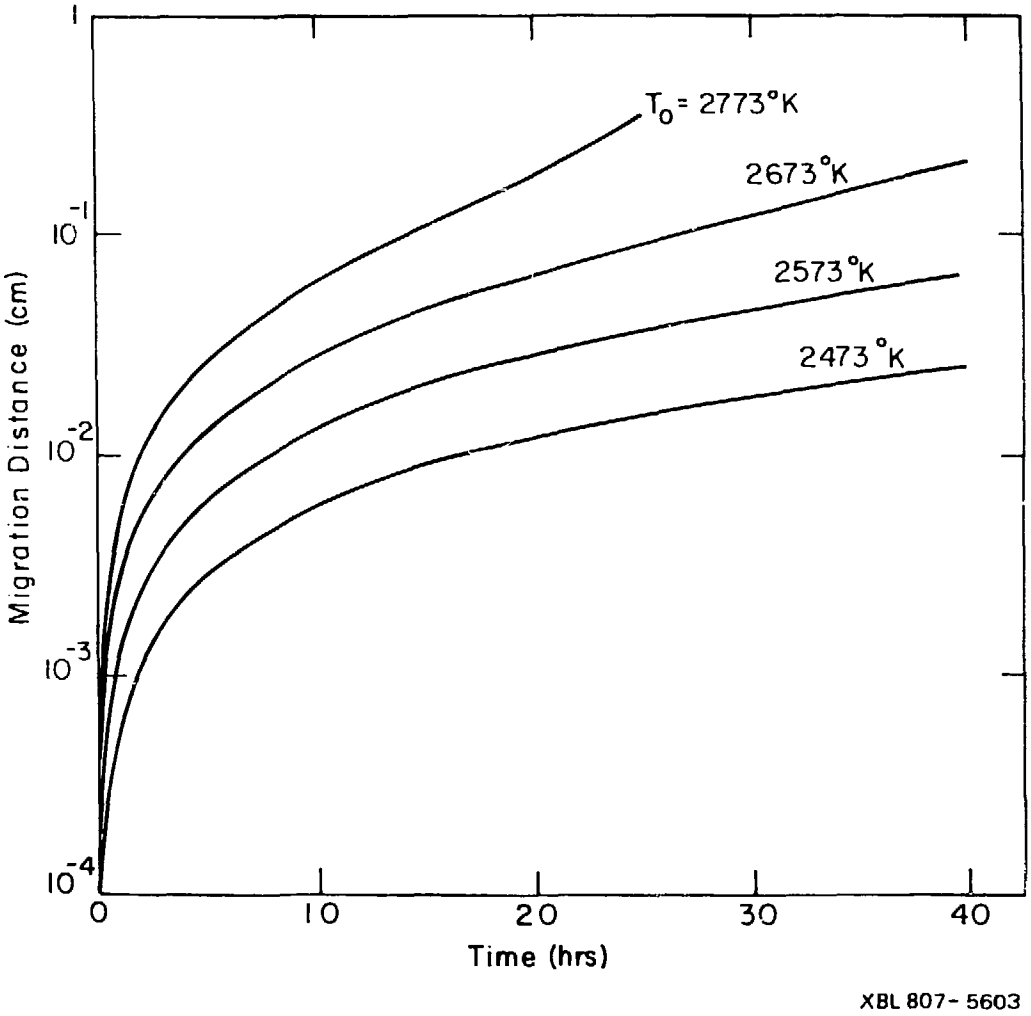

Fig. A-1. Migration distance (by surface diffusion mechanism) of a 5 μm tungsten inclusion as a function of time.